Raman resonance in iron-based superconductors: The magnetic scenario

Alberto Hinojosa, Jiashen Cai, and Andrey V. Chubukov

Phys. Rev. B **93**, 075106 — Published 4 February 2016

DOI: 10.1103/PhysRevB.93.075106

Raman resonance in iron-based superconductors: the magnetic scenario

Alberto Hinojosa,[1] Jiashen Cai,[1] and Andrey V. Chubukov[1]

[1]*Department of Physics, University of Minnesota, Minneapolis, Minnesota 55455, USA*

We perform theoretical analysis of polarization-sensitive Raman spectroscopy on $NaFe_{1-x}Co_xAs$, EuFe2As$_2$, $SrFe_2As_2$, and $Ba(Fe_{1-x}Co_x)_2As_2$, focusing on two features seen in the B_{1g} symmetry channel (in one Fe unit cell notation): the strong temperature dependence of the static, uniform Raman response in the normal state and the existence of a collective mode in the superconducting state. We show that both features can be explained by the coupling of fermions to pairs of magnetic fluctuations via the Aslamazov-Larkin process. We first analyze magnetically-mediated Raman intensity at the leading two-loop order and then include interactions between pairs of magnetic fluctuations. We show that the full Raman intensity in the B_{1g} channel can be viewed as the result of the coupling of light to Ising-nematic susceptibility via Aslamazov-Larkin process. We argue that the singular temperature dependence in the normal state is the combination of the temperature dependencies of the Aslamazov-Larkin vertex and of Ising-nematic susceptibility. We discuss two scenario for the resonance below T_c. One is the resonance due to development of a pole in the fully renormalized Ising-nematic susceptibility. Another is orbital excitonic scenario, in which spin fluctuations generate attractive interaction between low-energy fermions.

I. INTRODUCTION

Raman scattering in Fe-based superconductors has attracted substantial interest in the past few years due to the number of new features associated with multi-orbital/multi-band nature of these materials (see e.g., Refs. [1–7]). The subject of this paper is the theoretical analysis of the features in Raman scattering revealed by polarization-sensitive Raman spectroscopy in the normal and the superconducting states of Fe-based materials $NaFe_{1-x}Co_xAs$ (Ref. [9]), AFe_2As_2, A=Eu,Sr (Ref. [10]), and $Ba(Fe_{1-x}Co_x)_2As_2$ (Refs. [11, 12]). Polarized light was used to probe the Raman response in different symmetry channels, classified by the irreducible representations of the D_{4h} crystallographic point group [1]. In the normal state the real part of the (almost) static and uniform Raman susceptibility in the B_{1g} channel in one-iron unit cell notation (same as the B_{2g} channel in two-iron notation used in Refs. [9, 11]) is strongly temperature dependent – it increases below 300K roughly as $1/(T-T_0)$, where T_0 is positive at small doping, but changes sign and becomes negative above optimal doping. In the superconducting state the imaginary part of the B_{1g} Raman susceptibility displays a strong resonance-type peak at around 50 cm^{-1}. There is no such resonance peak in other channels, although the Raman intensity in the A_{1g} channel does show a broad maximum at a somewhat higher frequency (Ref. [9]).

In the effective mass approximation (in which the coupling of light to fermions is proportional to the square of vector potential) the measured Raman intensity in a particular channel (A_{1g}, B_{1g}, B_{2g}, ...) is proportional to the imaginary part of the fully renormalized particle-hole polarization bubble $\chi_R(\mathbf{p}, \Omega)$ with proper symmetry factors in the vertices, taken at vanishingly small transferred momentum $\mathbf{p}$ and finite transferred frequency Ω (Refs.[14],[15],[16]).

The free-fermion polarization bubble vanishes in the normal state for $\Omega > v_F p$, where v_F is the Fermi velocity, and obviously it cannot account for the observed strong temperature dependence of B_{1g} Raman intensity above T_c. It is non-zero in the superconducting state, but does not display a peak. The effect must then come from the renormalization of the Raman vertex due to coupling to some low-energy fluctuations (final state interaction in Raman literature [17]). This coupling may come from three different sources. First, the B_{1g} Raman vertex changes sign under $k_x \leftrightarrow k_y$ (i.e., under interchanging the x and y directions in real space), hence it couples to strain (structural fluctuations). Second, the B_{1g} vertex is anti-symmetric with respect to the interchange between the iron d_{xz} and d_{yz} orbitals and hence couples to orbital fluctuations. Third, symmetry allows the coupling between the B_{1g} Raman vertex and Ising-nematic spin fluctuations [the ones which distinguish between the magnitudes of spin-density-wave order parameters with ordering vectors $(0,\pi)$ and $(\pi,0)$] because both are anti-symmetric with respect to 90° rotations in the momentum space.

Structural fluctuations, orbital fluctuations, and Ising-nematic spin-fluctuations are the three key candidates to drive the nematic order, observed in most of the Fe-based materials. How to choose the primary candidate among these three has become one of the key issues in the studies of Fe-based superconductors[18]. We intend to verify whether the Raman data can help distinguish between the three candidates.

The effects of structural and orbital fluctuations has been discussed before (see Refs. [19], [20] and references therein). Structural fluctuations (acoustic phonons associated with strain) practically do not affect the Raman intensity because the coupling to phonons changes the B_{1g} Raman susceptibility $\chi_R(\mathbf{p}, \Omega)$ to

$$\tilde{\chi}_R(\mathbf{p}, \Omega) = \left[\chi_R^{-1}(\mathbf{p}, \Omega) - \frac{\lambda_{ph}^2 p^2}{C_{ph}^2 p^2 - \Omega^2}\right]^{-1}, \quad (1)$$

where λ_{ph} is electron-phonon coupling and C_{ph} is the elastic constant for orthorhombic strain. Such coupling is relevant in the static limit, where $\tilde{\chi}_R^{-1}(\mathbf{p},0) = \chi_R^{-1}(\mathbf{p},0) - (\lambda_{ph}/C_{ph})^2$ differs from $\chi_R^{-1}(\mathbf{p},0)$ by a constant term, but is irrelevant in the limit of vanishing p and finite Ω, where Raman measurements have been performed[9,11,12]. [In the B_{1g} channel the minimum p is, strictly speaking, non-zero[21], but is generally of order of inverse system size].

Orbital fluctuations do affect the B_{1g} Raman susceptibility via renormalizations involving particular combinations of intra-orbital and inter-orbital Hubbard and Hund terms, compatible with the fact that the B_{1g} Raman vertex changes sign between d_{xz} and d_{yz} orbitals. By orbital fluctuations we mean fluctuations which renormalize B_{1g} Raman vertex by inserting series of ladder and bubble diagrams, as shown schematically in Fig. 1 and in more detail in Figs. 17 and 18 in the Appendix.

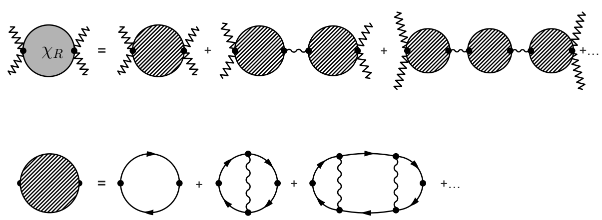

Figure 1. Ladder and bubble diagrams for the renormalization of the B_{1g} Raman intensity within RPA. Each combination of Green's fuunctions with equal momenta gives a particle-hole polarization bubble $\Pi_{B_{1g}}(\Omega)$ and the combination of vertical and horizontal interaction lines gives the coupling λ. We show We obtain λ explicitly in the Appendix for a system with dominant intra-orbital Hubbard interaction.

In the band basis, the interaction lines in these diagrams are Hubbard and Hund terms dressed by "coherence factors", associated with the transformation from the orbital to the band basis, and projected into B_{1g} channel. [Each interaction contains one incoming and one outgoing fermion with momentum $\mathbf{k}$ and one incoming and one outgoing fermion with momentum $\mathbf{p}$, and its B_{1g} component is proportional to $\cos 2\theta_k \cos 2\theta_p$, where $\tan\theta_k = k_y/k_x$]. In the approximation when only ladder and bubble diagrams are kept (often called random-phase approximation (RPA)), the Raman response in the B_{1g} channel is given by (see e.g., Ref. [22]),

$$\chi_R(\Omega) = \frac{\Pi_{B_{1g}}(\Omega)}{1+\lambda\Pi_{B_{1g}}(\Omega)}, \tag{2}$$

where $\chi_R(\Omega) = \chi_R(p \to 0, \Omega)$, λ is the proper combination of interactions in B_{1g} channel, and $\Pi_{B_{1g}}(\Omega)$ is the particle-hole polarization function at zero momentum transfer, summed over all bands with the B_{1g} form-factor. [We define $\Pi_{B_{1g}}(\Omega)$ as $-\int d^2k d\nu/(2\pi)^3 \times G(k,\nu)G(k,\nu+\Omega)$. With this sign convention, Re $\Pi_{B_{1g}}(\Omega)$ in a superconductor is positive at $\Omega < 2\Delta$, where Δ is the superconducting gap]. In the language of Fermi-liquid theory, $\lambda\Pi_{B_{1g}}(\Omega=0)$ is the B_{1g} component of the quasiparticle interaction function, and $\lambda\Pi_{B_{1g}}(\Omega=0) = -1$ would correspond to B_{1g} Pomeranchuk instability.

Because free-fermion $\Pi_{B_{1g}}(\Omega)$ vanishes in the normal state (the poles of both Green's functions are in the same frequency half-plane), Eq. (2) cannot explain the normal state behavior of the Raman response. However, $\chi_R(\Omega)$ from Eq. (2) is non-zero in a superconductor, because $\Pi_{B_{1g}}(\Omega)$ becomes non-zero, and for negative λ it displays a resonance peak. The resonance develops by the same reason as the excitonic spin resonance in a $d-$wave superconductor[23]: the imaginary part of the polarization function $\Pi(\Omega)$ vanishes for $\Omega < 2\Delta$, while the real part of $\Pi(\Omega)$ is positive and diverges at $\Omega = 2\Delta$. As the result, for negative λ, the denominator in (2) is guaranteed to pass through zero at some frequency below 2Δ, and a sharp resonance in $\chi_R(\Omega)$ appears at this frequency[22].

This would be the most natural explanation of the Raman resonance. The problem, however, is how to justify that λ is negative, i.e., that there is an attraction in the B_{1g} ($d-$wave) charge Pomeranchuk channel. If intra-orbital Hubbard repulsion is the dominant interaction term, λ is definitely positive and orbital fluctuations do not give rise to the resonance in the Raman intensity (we show this in the Appendix). The coupling λ does become negative when inter-orbital interaction U' and exchange Hund interaction J are included and U' is set to be about equal to U and larger than J (Ref. [24]).

However, the relation $U' \approx U$ gets broken once one starts integrating out high energy fermonic excitations (Ref. [25]) or includes lattice effects (Ref. [26])

In a generic case it is natural to expect that the intra-orbital Hubbard interaction is the strongest interaction between Fe $d-$orbitals. If so, the coupling λ is positive and there is no resonance in $\chi_R(\Omega)$ within RPA.

In this paper we analyze whether the increase of $\chi_R(\Omega)$ in the B_{1g} channel in the normal state and the sharp peak in the Raman response in this channel below T_c can be due to Ising-nematic spin fluctuations associated with stripe magnetism. The advantage of the magnetic scenario is that Ising-nematic fluctuations are enhanced even when intra-orbital Hubbard interaction is the dominant interaction between fermions. The only requirement is that the magnetic order should be stripe rather than checkerboard.[27]

The coupling of the Raman vertex to a pair of spin fluctuations with momenta near $\mathbf{Q} = (0,\pi)$ [or $(\pi,0)$] occurs via the Aslamazov-Larkin (AL) process. The corresponding diagram is presented in Fig. 2. AL diagrams for Raman scattering have been earlier discussed in Ref. [28], but in a different context. The lowest-order AL type diagram (the one shown in Fig. 2) contains two triangular vertices made out of fermionic Green's functions from hole and electron bands, and two spin-fluctuation propagators. The vertex between fermions and spin fluctuations can be obtained by decomposing the antisymmetrized interaction into spin and charge parts, by focusing on spin-spin part, and by using Hubbard-Stratonovich method to transform interaction between fermionic spins into spin-spin interaction between a fermion and a collective bosonic variable in the spin channel[27].

We show that in the normal state, above a certain temperature, each triangular vertex Γ_{tr} scales as $1/T$, while the convolution of the two spin propagators at equal frequencies (i.e. $T\sum_\nu \int d^2q(\chi^s(Q+q,\nu))^2$) scales as T. As the consequence, the Raman susceptibility from Fig. 2 scales as $1/T$. This holds in both A_{1g} and B_{1g} channels. Higher-order processes, shown in Fig. 3 and in more detail in Fig. 6 below, however, distinguish between A_{1g} and B_{1g} Raman responses. Namely, an attractive interaction between magnetic fluctuations in the B_{1g} channel increases B_{1g} Raman response and changes $1/T$ dependence into $1/(T-T_0)$ (see Refs. [29, 30] and Sec.III below), while the (much stronger) repulsive interaction in the A_{1g} channel almost completely eliminates the temperature dependence of A_{1g} Raman response. This behavior fully agrees with the data.

In the superconducting state, the $1/T$ behavior of Γ_{tr} is cut by the gap opening, while $\chi^2(\Omega) = T\sum_\mu \int d^2q\chi^s(q+Q,\nu)\chi^s(q+Q,\nu+\Omega)$ becomes singular. The real part of $\chi^2(\Omega)$ diverges at $\Omega = 2\Omega_{\rm mag}$, where $\Omega_{\rm mag}$ is the minimal frequency of the magnetic resonance in the superconducting state, and its imaginary part jumps at this frequency from zero to a finite value. Higher-order terms change $\chi^2(\Omega)$ into $\chi_{I-nem}(\Omega) = \chi^2(\Omega)/(1+2g\chi^2(\Omega))$ (see Sec. III), where g is negative (attractive) when magnetic order is of stripe type[27]. Approximating the triangular vertex Γ_{tr} by a constant we then obtain

$$\chi_R(\Omega) = \Gamma_{tr}^2\chi_{I-nem}(\Omega) = \Gamma_{tr}^2\,\frac{\chi^2(\Omega)}{1+2g\chi^2(\Omega)}. \quad (3)$$

The combination of $g<0$ and the fact that the real part of $\chi^2(\Omega)$ is positive and diverges at $\Omega = 2\Omega_{\rm mag}$ guarantees that $1+2g\chi^2(\Omega)$ passes through zero at some $\Omega = \Omega_{res,1} < 2\Omega_{\rm mag}$. At this frequency the Raman intensity Im $\chi_R(\Omega)$ displays a δ-functional peak.

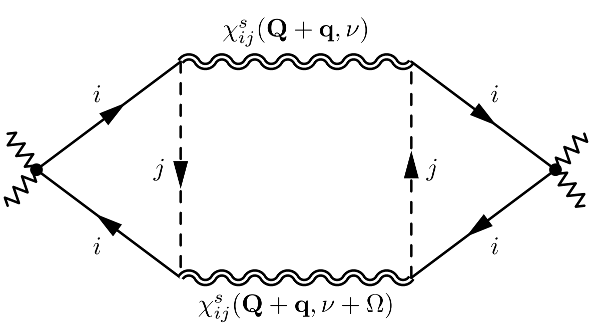

Figure 2. The lowest order (two-loop) AL diagram for the Raman intensity. The momenta $Q_1 = (\pi, 0)$ and $Q_2 = (0, \pi)$. The solid and dashed lines represent fermions from different bands with band indices i and j. The sinuous lines represent spin fluctuations and the external jagged lines are the coupling to photons.

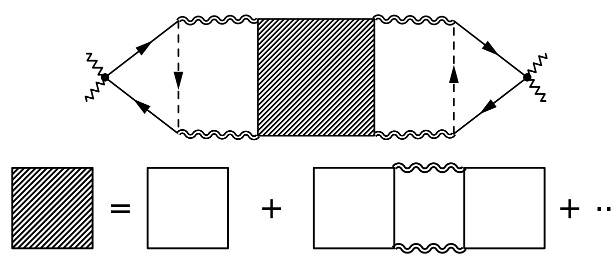

Figure 3. Schematic representation of higher-order contributions to the Raman response. We show higher-order terms in more detail in Fig. 6.

We show that approximating Γ_{tr} by a constant is justified if typical fermionic frequencies in the triangular diagram for Γ_{tr} are larger than Ω_{mag}. These relevant frequencies are of order Δ, hence the analysis is justified when $\Omega_{mag} \ll \Delta$. This holds if the inverse magnetic correlation length m_s is small enough because $\Omega_{mag} \propto m_s$ (Ref. [31]). In the Fe-based materials, in which B_{1g} resonance has been observed, the situation is, however, somewhat different: neutron scattering data for $\text{NaFe}_{1-x}\text{Co}_x\text{As}$ with $x = 0.045$ show[32] that $\Omega_{\rm mag} \approx 7$ meV, while $\Delta = 5 - 5.5meV$ (Ref. [33], i.e. Δ is somewhat smaller than Ω_{mag}. In this situation, there is no good reason to treat Γ_{tr} as a constant, independent on Ω_{mag}, because two fermionic frequencies in the triangular loop differ by Ω_{mag}.

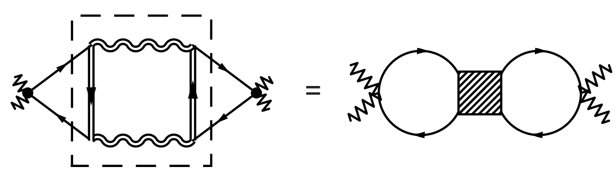

Figure 4. Interpretation of the two-loop AL diagram as consisting of two particle-hole bubbles with zero momentum transfer (unshaded circles), separated by the magnetically-mediated 4-fermion interaction. The notations are the same as in Fig. 2. Higher-order terms are shown in Fig. 8.

In view of this complication, we also analyze another scenario for the B_{1g} resonance below T_c, namely that the resonance originates from the 2Δ singularity of the particle-hole polarization $\Pi_{B_{1g}}(\Omega)$ in an $s-$wave superconductor, like in the "pure" orbital fluctuation scenario, while spin fluctuations renormalize the original, likely repulsive, coupling λ in Eq. (2) into the effective coupling $\lambda_{\rm eff}$ (see Figs. 4). This scenario is justified in the opposite limit when Ω_{mag} is assumed to be much larger than Δ. The strong inequality never holds because $\Omega_{mag} < 2\Delta$, but weak inequality may be already enough number-wise. We show that λ_{eff} turns out to be negative (i.e., attractive) near a nematic instability. For negative $\lambda_{\rm eff}$, $1+\lambda_{\rm eff}\Pi_{B_{1g}}(\Omega)$ necessary vanishes at some frequency $\Omega_{res,2}$ below 2Δ, where Im$\Pi_{B_{1g}}(\Omega)$ is zero, and this leads to an excitonic-type resonance in the B_{1g} Raman response.

Such a scenario has been proposed in earlier works[12,22] based on the phenomenological argument that Ising-nematic and orbital order parameters break the same C_4 symmetry and hence are linearly coupled in the Landau functional. A bilinear term with a constant prefactor A was argued to give rise to the renormalization of λ into $\lambda_{\text{eff}} = \lambda - A^2\chi_{I-nem}$. The latter is obviously negative when χ_{I-nem} is large. We compute the renormalization of λ within our microscopic model. We show that λ_{eff} does become negative and scales as χ_{I-nem}. However prefactor is not A^2 and is non-zero only if one includes the non-analytic dynamical Landau damping term into the spin propagator. If spin-fluctuation propagator is approximated by its static part, $\lambda_{eff} = 0$. We explain the difference between the coupling between Pomeranchuk order parameter and two spin fluctuations (=A) and between Ising-nematic and orbital (Pomeranchuk) order parameters, which actually gives rise to the renormalization of λ.

The outcome of this study is that the resonance in B_{1g} Raman intensity is of purely magnetic origin at $\Omega_{mag} \ll \Delta$ – it is due to the pole in $\chi_{I-nem}(\Omega)$ at $\Omega_{res,1}$. At $\Omega_{mag} > \Delta$ the resonance of fermionic origin – it develops by the same reason as in purely orbital scenario, due to the emergence of the excitonic pole in the ladder series of particle-hole bubbles with B_{1g} vertices. However, the attraction between fermions in the B_{1g} channel comes from magnetically-mediated interaction.

In FeSCs, Ω_{mag} and Δ are comparable, in which case the actual resonance is likely the mixture of the nematic and the excitonic resonances. In $NaFe_{1-x}Co_xAs$ with $x = 0.045$, the B_{1g} peak is seen at 7.1 meV (Ref. [9]), which is below both 2Δ and $2\Omega_{mag}$.

The paper is organized as follows: In Sec. II we evaluate analytically the two-loop AL-type diagram for B_{1g} Raman scattering. In Sec. III we show that in the normal state this contribution to $\chi_R(\Omega)$ is strongly temperature dependent. The temperature dependence is roughly $1/T$. We argue that higher-order terms, which include interactions between pairs of spin fluctuations, replace $1/T$ dependence into more singular $1/(T - T_0)$. In Sec. IV we extend the analysis to the superconducting state. In Sec. IV A we argue that spin excitations with momenta near $(0, \pi)$ and $(\pi, 0)$ evolve below T_c and become magnon-like, with minimal energy Ω_{mag}. We compute two-loop AL diagram assuming that the vertices which couple light to spin fluctuations saturate below T_c, and show that this contribution to Raman intensity becomes logarithmically singular at $\Omega = 2\Omega_{mag}$. We further show that higher-order terms, which include interactions between spin fluctuations, convert logarithmical singularity at $2\Omega_{mag}$ into a true resonance peak at an energy $\Omega_{res,1} < 2\Omega_{mag}$. In Sec. IV B we re-interpret the two-loop AL diagram for B_{1g} Raman scattering differently, as the contribution from two particle-hole polarization bubbles with an effective interaction mediated by spin fluctuations. We compute the magnetically-mediated 4-fermion interaction λ_{mag} and show that it is attractive. We argue that higher-order terms give rise to an excitonic peak in $\chi_R(\Omega)$ at $\Omega_{res,1}$ below 2Δ. In Sec. IV C we discuss the interplay between this peak and the one coming from fully renormalized nematic susceptibility. In Sec. IV D we present the results of numerical computation of spin-fluctuation contribution to Raman intensity at two-loop and higher orders. In Sec. V we compare AL vertices for the coupling to spin fluctuations in different symmetry channels and show that in the B_{2g} channel (in the 1Fe zone) the vertex for the coupling of light to spin fluctuations vanishes by symmetry. The vertex in A_{1g} channel does not vanish and is of the same order as the vertex in B_{1g} channel. We show, however, that there is no resonance in A_{1g} because the interaction between spin fluctuations in this channel is strongly repulsive instead of attractive. We present our conclusions in Sec. VI.

Throughout the paper we will be using band formalism and will be working in the 1-Fe Brillouin zone (BZ).

II. RAMAN RESPONSE FROM SPIN FLUCTUATIONS

We consider the four-band model of $NaFe_{1-x}Co_xAs$ and $(Fe_{1-x}Co_x)_2As_2$ with two hole pockets centered at $k_x = k_y = 0$ and two electron pockets centered at $(0, \pi)$ and $(\pi, 0)$ in the 1 Fe Brillouin zone (BZ), see Refs. [35–38]. Excitations near the hole pockets are composed out of d_{xz} and d_{yz} orbitals and there is 90^o rotation of the orbital content near one Fermi surface compared to the other. Excitations near electron pockets are predominantly composed out of d_{xy} and d_{xz} orbitals for the $(0, \pi)$ pocket and out of d_{xy} and d_{yz} orbitals for the $(\pi, 0)$ pocket[13]. We do not include into consideration the third hole pocket, centered at (π, π) in the 1Fe zone, as it is made out of C_4-symmetric d_{xy} orbital and doesn't play any significant role in the analysis of Raman scattering, particularly in B_{1g} geometry.

The Raman response function can be calculated as a time-ordered average of density operators weighted with Raman form-factors:

$$\chi_R(\mathbf{p}, \Omega) = -i \int \mathrm{d}t e^{i\Omega t} \left\langle T \rho_{\mathbf{p}}(t) \rho_{-\mathbf{p}}(0) \right\rangle, \tag{4}$$

where

$$\rho_{\mathbf{p}} \equiv \sum_{i,\mathbf{k},\sigma} \gamma_i(\mathbf{k}) c^\dagger_{i,\mathbf{k}+\mathbf{p},\sigma} c_{i,\mathbf{k},\sigma}. \tag{5}$$

Here i represents a band index, σ represents a spin projection of a fermion, and $\gamma(\mathbf{k})$ is the Raman form-factor which keeps track of the polarizations of the incoming and the outgoing light. The use of light of different polarizations allows the probing of different symmetry channels: A_{1g}, A_{2g}, B_{1g} and B_{2g}. Note that the B_{1g} and B_{2g} channels are interchanged when going from the 1-Fe BZ to the 2-Fe BZ, because the coordinate system is rotated $45°$ to make the k_x and k_y axes coincide with the sides of the square cell. Because the wavelength of light used in the experiments is a few orders of magnitude greater than the lattice constant, the typical values of $v_F p$ are smaller than typical Ω, and it suffices to calculate the susceptibility at $p \to 0$ i.e., compute $\chi_R(\Omega) \equiv \chi_R(p \to 0, \Omega)$.

Without the final state interaction, the Raman response involving a pair of spin fluctuations with momenta near $(0, \pi)$ and $(\pi, 0)$ (the difference between the centers of electron and hole pockets) is given by the diagram shown in Fig. 2. Since light can couple to each hole and electron band, there are several diagrams of this kind with two fermionic lines from one of hole pockets or from one of electron pockets (see Fig. 16 below). The combined contribution from these diagrams takes the form

$$\chi_R(\Omega) = -i \int \frac{d^2\mathbf{q} d\nu}{(2\pi)^3} \Gamma^2_{tr,l}(\mathbf{q}, \nu) f_l \chi^s(\mathbf{Q}_l + \mathbf{q}, \nu) \times \chi^s(\mathbf{Q}_l + \mathbf{q}, \nu + \Omega), \tag{6}$$

where $\Gamma_{tr,l}$ defines the vertex for the coupling between light and spin fluctuations (see Fig. 5), χ^s is the propagator of spin fluctuations, $l = 1, 2$ with $Q_1 = (\pi, 0)$, $Q_2 = (0, \pi)$, and f_l is the symmetry factor, e.g., $f_l = \sigma^z_{ll}$ for B_{1g} geometry.

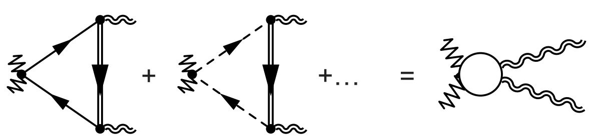

Figure 5. The AL vertex Γ_{tr} for the coupling of light to spin fluctuations. Single solid and dashed lines represent excitations from one of the two hole bands and the double solid line represents excitations from one of the two electron bands. When typical internal frequencies in the triangle made out of fermionic Green's functions are larger than typical frequencies of spin fluctuations, Γ_{tr} can be approximated by a constant (a circle on the r.h.s of the figure).

The vertex $\Gamma_{tr,l}(q, \nu)$ is composed out of three fermionic Green's functions, the Raman factor $\gamma(k)$, and two vertices for the coupling between fermions and spin-fluctuations: $g_{sf}\gamma_{ij}(k, k + Q_l - q)$, where g_{sf} is the spin-fermion coupling (or order of the intra-orbital Hubbard U) and $\gamma_{ij}(k, k + Q_i - q)$ are coherence factors associated with the transformation from orbital to band basis for fermions from bands i and j $(i, j = 1, 2)$. In a superconducting state one must include diagrams containing anomalous Green's functions, which create or destroy particles in pairs, and sum over all allowed combinations of normal and anomalous functions. For any particular combination of normal and anomalous functions, the triangular vertex takes the form

$$\Gamma_{tr,l}(\mathbf{q}, \nu) = g^2_{sf} \int \frac{d^2\mathbf{k} d\omega}{(2\pi)^3} \gamma_i(\mathbf{k}) \gamma^2_{ij}(k, k + Q_l - q) \tilde{G}_i(\mathbf{k}, \omega) \tilde{G}_i(\mathbf{k}, \omega + \Omega) \tilde{G}_j(\mathbf{k} + \mathbf{Q}_l - \mathbf{q}, \omega - \nu), \tag{7}$$

where $\tilde{G}_{i,j}$ are either normal (G) or anomalous (F) Green's functions with i from a hole pocket and j from an electron pocket or vice versa. The index of the electron band is equal to l.

III. THE VERTEX FUNCTION IN THE NORMAL STATE AND THE TEMPERATURE DEPENDENCE OF THE B_{1g} SUSCEPTIBILITY ABOVE T_c

In this Section we compute the Raman vertex function in the normal state and obtain the temperature dependence of the real part of the Raman susceptibility in the static limit. Here and in Sec. IV we focus on B_{1g} scattering geometry with $\gamma(\mathbf{k}) \propto \cos \mathbf{k_x} - \cos \mathbf{k_y}$ and do not explicitly write symmetry factors in the Raman vertex and in the vertices relating fermions with spin fluctuations. We will discuss these symmetry factors and different geometries in Sec. V. We also neglect for simplicity the eccentricity of the electron pockets and set all Fermi surfaces to be circles of the same size. This approximation simplifies calculations, but does not qualitatively affect the temperature dependence compared to a generic case in which the pockets are different. In the static limit Eq. (7) in the normal state reduces to

$$\Gamma_{tr}(\mathbf{q}, \nu_n) = -AT \sum_{\omega_m} \int \frac{d^2\mathbf{k}}{(2\pi)^2} \frac{1}{(i\omega_m - \xi^i_{\mathbf{k}})^2} \frac{1}{i(\omega_m - \nu_n) - \xi^j_{\mathbf{k}-\mathbf{q}}} \tag{8}$$

where $A \sim g^2_{sf}$. For concreteness we assume that i is a hole band and j is an electron band. The hole and electron dispersions are given by $\xi^i_{\mathbf{k}} = \mu - \frac{k^2}{2m} = -\xi^j_{\mathbf{k}}$, where μ is the chemical potential. At $\mathbf{q} = 0$ and $\nu_m = 0$, Γ_{tr} is given by

$$\Gamma_{tr} = \frac{Am}{16\pi T} f\left(\frac{\mu}{2T}\right).$$

The scaling function $f(x) = \tanh(x)/x$ is close to 1 for $x < 1$, i.e., for $T > \mu/2$. In this temperature range $\Gamma_{tr} \approx Am/(16\pi T)$ scales as $1/T$. This has been noticed before[39]. At larger x (smaller T), Γ_{tr} tends to a constant.[30] At a non-zero $\mathbf{q} = 0$ and ν_m the expression for Γ_{tr} becomes more complex, but as long as $\nu_m = O(T)$ and $|\mathbf{q}| \leq k_F$, the functional form remains the same.

We next compute the convolution of two spin fluctuations in the normal state. There is no controllable way to obtain the spin-fluctuation propagator starting from the fermion-fermion interaction. The RPA procedure is often used, but it selects particular series of ladder and bubble diagrams in the particle-hole channel and neglects contributions from the particle-particle channel. The latter are, however, not small, even at perfect nesting[40]. Besides, in a general case of hole and electron pockets of different sizes and geometry, the static propagator of spin fluctuations comes from fermions with energies of order bandwidth, for which the low-energy expansion is not applicable. In view of this complication, we adopt the same approach as in earlier works on the spin-fermion model[41] and assume phenomenologically that the static part of the spin-fluctuation propagator has a regular Ornstein-Zernike form $\chi^s_{ij}(\mathbf{q}+\mathbf{Q},0) = 1/(q^2+m_s^2)$, where m_s is the inverse magnetic correlation length (the overall factor in χ^s is incorporated into the spin-fermion coupling). The dynamical part of χ^s, however, comes from low-energy fermions and can be obtained by computing the dynamical part of particle-hole polarization bubble made of fermions near a hole and an electron pocket, separated by Q. Then

$$\chi^s(\mathbf{Q}+\mathbf{q},\nu_m) = \frac{1}{m_s^2+q^2+\gamma\Pi_Q(\nu_m)}, \tag{9}$$

where $\gamma = mg_{sf}/(2\pi)$, g_{sf} is the spin-fermion coupling (Ref. [41]), and $\Pi_Q(\nu_m) = \Pi(\mathbf{Q},\nu_m) - \Pi(\mathbf{Q},0)$, where $\Pi(\mathbf{Q},\nu_m)$ is the dynamical polarization bubble at momentum transfer $\mathbf{Q}$. The polarization bubble $\Pi_Q(\nu_m)$ is logarithmic in ν_m because it is the convolution of fermions from hole and electron bands with opposite sign of the dispersion[43]. We computed $\Pi_Q(\nu_m)$ numerically and found that it can be well approximated by

$$\Pi_Q(\nu_m) = \log\left(3.57\frac{|\nu_m|}{2\pi T}\right) \tag{10}$$

starting already from the lowest non-zero Matsubara frequency. Substituting this into (9) and evaluating the convolution of the two dynamical spin susceptibilities with the same momentum and frequency we obtain

$$\begin{aligned} &T\sum_{\nu_m}\int\frac{\mathrm{d}^2\mathbf{q}}{(2\pi)^2}\chi^s(\mathbf{q}+\mathbf{Q},\nu_m)\chi^s(\mathbf{q}+\mathbf{Q},\nu_m) \\ &\propto T(m_s)^{-2}\left(1+\sum_{m\neq 0}\frac{1}{1+\gamma(m_s)^{-2}\log(3.57|m|)}\right) \end{aligned} \tag{11}$$

The coupling constant γ cannot be calculated within the theory, but is generally of order 1. Assuming that this is the case, we find that the dominant contribution to the sum over bosonic Matsubara frequencies comes from the term with $\nu_n = 0$, at least when the inverse magnetic correlation length $m_s < 1$. The convolution of the two χ^s then gives, up to a constant prefactor, T/m_s^2 (Ref. [20]). Combining this with $\Gamma^2_{tr} \propto 1/T$, we obtain that the contribution to the static B_{1g} Raman susceptibility from the processes involving a pair of spin fluctuations with momenta near $(0,\pi)$ and $(\pi,0)$ and two triple vertices (i.e., from the diagram in Fig. 2) is given by

$$\chi_R(\Omega=0) \propto \frac{1}{Tm_s^2} \tag{12}$$

Outside the T range near a magnetic transition, the temperature dependence of m_s is weak, and $\chi_R(\Omega=0)$ scales roughly as $1/T$.

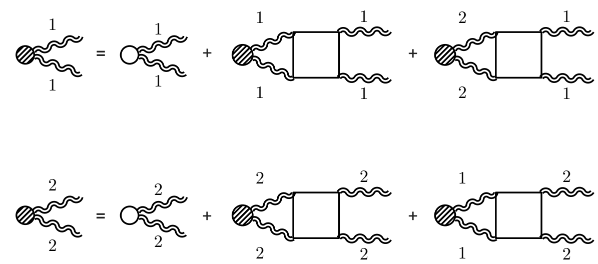

Figure 6. Ladder series of renormalizations of the interaction of light with spin fluctuations with momenta near $Q_1 = (\pi,0)$ (labeled as 1) and near $Q_2 = (0,\pi)$ (labeled as 2). The interaction vertices are made out of fermions from different bands (see Fig. 7).

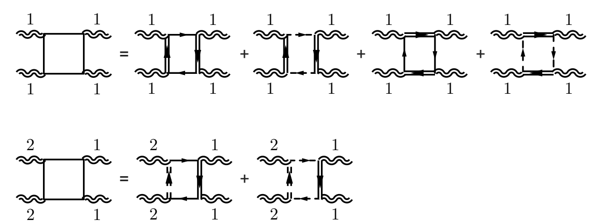

Figure 7. The structure of the vertices for the interaction between spin fluctuations with near $Q_1 = (\pi,0)$ (labeled as 1) and near $Q_2 = (0,\pi)$ (labeled as 2). The single solid and dashed lines represent excitations from one of the two hole bands and the double solid and dashed lines represent excitations from one of the two electron bands.

A. Higher-order contributions to Raman susceptibility

We next consider how Eq. (12) changes once we include the interactions between pairs of spin fluctuations. These interactions either leave bosonic momenta near a particular $Q_1 = (\pi,0)$ or $Q_2 = (0,\pi)$, or transfer both momenta from Q_1 to Q_2 or vice versa. In the latter case, the process belongs to umklapp category and is allowed because $2Q_1 = 2Q_2$ up to reciprocal lattice vector. We show the corresponding diagrams in Fig. 6. Each interaction vertex is given by the convolution of four fermionic propagators (see Fig. 7). These vertices have been computed in Ref. [27] in the limit when bosonic frequencies are set to zero. We argued above that this approximation is justified for the two-loop diagram, and we now assume that this also holds for higher-order processes. We then borrow the results from Ref. [27], which demonstrated that the effective interaction in the B_{1g} channel is a *negative* (attractive) $2g$, which scales with temperature as $1/T^4$.

We show explicitly how to solve the coupled set of ladder equations for the fully renormalized AL vertices with momenta Q_x and Q_y later in Sec. V (where we compare A_{1g} and B_{1g} channels), because the set involves both A_{1g} and B_{1g} components. Here we just present the result: at small Ω, interactions between spin-fluctuations change the two-loop AL Raman vertex in B_{1g} geometry into

$$\chi_R(\Omega) = \Gamma_{tr}^2 \frac{\chi^2(\Omega)}{1+2g\chi^2(\Omega)} = \Gamma_{tr}^2 \; \chi_{I-nem}(\Omega), \qquad (13)$$

where $\chi^2(\Omega)$ is the short-notation for the convolution of two spin-fluctuation propagators with relative frequency Ω) and we defined

$$\chi_{I-nem}(\Omega) = \frac{\chi^2(\Omega)}{1+2g\chi^2(\Omega)} \qquad (14)$$

Using $g \sim 1/T^4$, $\chi^2 \propto T$, $\Gamma_{tr} \propto 1/T$ and introducing T_0 as a temperature at which $2g\chi^2 = 1$, we obtain

$$\chi_R(0,T) \sim \frac{(m_s)^{-2}}{T-T_0} \left(\frac{T^2}{T^2+TT_0+T_0^2} \right) \qquad (15)$$

which for $T > T_0$ is rather well approximated by

$$\chi_R \sim \frac{1}{T-T_0}, \qquad (16)$$

In Sec. V we show that singular $1/(T-T_0)$ dependence only holds for the B_{1g} Raman vertex. In other channels, Raman intensity from the coupling to spin fluctuations either vanishes by symmetry of is substantially reduced by interaction between spin-fluctuations.

The $1/(T-T_0)$ behavior of the B_{1g} Raman vertex is quite consistent with the experimental observations for $NaFe_{1-x}Co_xAs$, $EuFe_2As_2$, and $Ba(Fe_{1-x}Co_x)_2As_2$ [9–12] In these materials T_0 is positive at doping below a certain x_0. This T_0 would be the temperature of Ising-nematic instability in the absence of (i) superconductivity and (ii) coupling to phonons. Superconductivity obviously cuts $1/(T-T_0)$ behavior at T_c, if T_c is larger than T_0. The coupling to static phonons shifts the the coupling g to $g_{eff} = g + (\Gamma_{tr}\lambda_{ph}/C_{ph})^2/2$ (see Eq. (1) and hence shifts the temperature of the Ising-nematic instability to $T_{nem} > T_0$. We remind that this shift is not present in the "static" χ_R, extracted from the measured Im $\chi_R(\Omega)$ by Kramers-Kronig transformation, because the contribution from phonons rapidly drops at non-zero Ω and is negligibly small for frequencies at which Im $\chi_R(\Omega)$ has been measured. As a result, "static" B_{1g} susceptibility extracted from the Raman data increases upon decreasing T but does not diverge even at T_{nem}.

Note also that T_0 is positive as long as magnetic order is a stripe, otherwise $g > 0$ and final state interaction reduces rather than enhances the Raman intensity. Recent studies have shown[42] that g does change sign as doping increases, hence one should expect that T_0 will change sign from positive to negative above a cerain doping. This is fully consistent with the data.[9]

IV. THE RESONANCE IN B_{1g} CHANNEL BELOW T_c

We now turn to the superconducting state. We first argue in Sec. IV A that under certain conditions the resonance in B_{1g} Raman response is due to the development of the pole in $\chi_{I-nem}(\Omega)$, given by (14). In Sec. IV B we consider another scenario for the resonance. Namely, we re-interpret the two-loop diagram as containing two dynamical particle-hole polarization bubbles with zero momentum transfer, $\Pi_{B_{1g}}(\Omega)$, coupled by an effective interaction mediated by spin fluctuations (see Figs. 4, 8). This effective interaction renormalizes λ in Eq. 2 into λ_{eff}, and we show that λ_{eff} becomes negative. Like we said in the Introduction, for negative coupling the system develops an excitonic resonance in the superconducting state, at a frequency below twice the superconducting gap.

A. Resonance due to the pole in χ_{I-nem}

To analyze the form of χ_{I-nem} at $T = 0$ in a superconductor we need to know the form of $\chi^s(\mathbf{Q}+\mathbf{q},\nu)$ along the real frequency axis. As in earlier works, we assume that the symmetry of the superconducting order parameter is s^{+-}. Superconductivity does not affect the static form of χ^s as it generally comes from high-energy fermions, but changes the form of the dynamical term $\Pi_Q(\nu) = \Pi_s(\mathbf{Q},\nu) - \Pi_s(\mathbf{Q},0)$ in Eq. (9) (converted to real frequencies), as this term now contains the sum of G_sG_s and F_sF_s terms. Approximating fermionic dispersion in the same way as before we obtain

$$\Pi_s(\mathbf{Q},\nu) = \frac{1}{2}\int \frac{d^2\mathbf{k}}{(2\pi)^2} \left[\frac{1}{\nu + 2E_{\mathbf{k}} - i\eta} - \frac{1}{\nu - 2E_{\mathbf{k}} + i\eta} \right], \qquad (17)$$

where $E_{\mathbf{k}}^2 = \xi_{\mathbf{k}}^2 + \Delta^2$ and $\xi_{\mathbf{k}} = \mu - \frac{k^2}{2m}$ (note that we define Π without a spin factor of 2). In principle, in evaluating $\Pi_s(\mathbf{Q},\nu)$ one has to include also G_sF_s terms and combine renormalizations in the particle-hole and the particle-particle channels because in the superconducting state particles and holes are mixed[44]. Previous work on the subject[45], however, has shown that as long as all the interactions are repulsive, the effect of inclusion of these extra terms is minimal in the case of Fe-pnictides and merely shifts the resonance frequency (see below) down by a few percentage points.

The straightforward analysis shows that $\mathrm{Im}\,\Pi_Q(\nu)$ vanishes for $|\nu| < 2\Delta$ because the excitations are gapped. At $|\nu| = 2\Delta$, $\mathrm{Im}\,\Pi_Q(\nu)$ undergoes a discontinuous jump to a finite value and $\mathrm{Re}\,\Pi_Q(\mu)$ diverges logarithmically. The divergence of the real part of $\Pi_Q(\nu)$ at $\nu = 2\Delta$ implies that the denominator in (9) must vanish at some frequency below 2Δ, thus creating a pole in $\chi^s(\mathbf{Q}+\mathbf{q},\nu)$. Specifically, for a given $\mathbf{q}$, $\mathrm{Im}\,\chi^s(\mathbf{Q}+\mathbf{q},\nu)$ has sharp peak at frequency $\nu_{\rm res}(\mathbf{q})$ and $\mathrm{Re}\,\chi^s(\mathbf{Q}+\mathbf{q},\nu)$ diverges. This is indeed nothing but the spin resonance in an s^{+-} superconductor.[46] Because time-ordered $\Pi_Q(\nu)$ is an even function of ν, it follows that for a given $\mathbf{q}$, time-ordered $\chi^s(\mathbf{Q}+\mathbf{q},\nu)$ has two simple poles at $\nu =$

$\pm\nu_{\rm res}(\mathbf{q})$. Then χ^s can be written as

$$\chi^s(\mathbf{Q}+\mathbf{q},\nu) = \frac{a(\mathbf{q},\nu)}{(\nu+\nu_{\rm res}(\mathbf{q}))(\nu-\nu_{\rm res}(\mathbf{q}))} \tag{18}$$

where $a(\mathbf{q},\nu)$ is some analytic function which is also even in ν.

We now turn to the Raman susceptibility from the two-loop diagram, Eq. (6). We assume and then verify that the triangular Raman vertex Γ_{tr} can be approximated by a constant and taken out of the integral for χ_R. The $1/T$ temperature dependence of Γ_{tr} is obviously cut by T_c, i.e., it remains finite at $T=0$. Whether it can be taken out of the integral over the bosonic frequency is a more subtle issue and we discuss it at the end of this Section.

With Γ_{tr} approximated by a constant, the expression for the Raman susceptibility takes the form

$$\chi_R(\Omega) = \Gamma_{tr}^2\chi^2(\Omega) \tag{19}$$

where

$$\chi^2(\Omega) = -i\int\frac{d^2\mathbf{q}d\nu}{(2\pi)^3}\sigma^z_{ii}\chi^s(\mathbf{Q}_i+\mathbf{q},\nu)\chi^s(\mathbf{Q}_i+\mathbf{q},\nu+\Omega). \tag{20}$$

where we remind that $i=1,2$, $Q_1=(\pi,0), Q_2=(0,\pi)$, and σ^z_{ii} is present because we consider B_{1g} geometry.

Substituting χ_s from (18) into Eq. (20) and evaluating the frequency integral, we obtain, neglecting symmetry factors,

$$\chi^2(\Omega) = -\int\frac{d^2\mathbf{q}}{(2\pi)^2}\frac{a(\mathbf{q},\nu_{\rm res}(\mathbf{q}))}{2\nu_{\rm res}(\mathbf{q})\Omega} \tag{21}$$

$$\times\left[\frac{a(\mathbf{q},\Omega-\nu_{\rm res}(\mathbf{q}))}{\Omega-2\nu_{\rm res}(\mathbf{q})}+\frac{a(\mathbf{q},\Omega+\nu_{\rm res}(\mathbf{q})}{\Omega+2\nu_{\rm res}(\mathbf{q})}\right]. \tag{22}$$

This formula shows that for each momentum $\mathbf{q}$ there is an enhancement of the response at twice the frequency $\nu_{\rm res}(\mathbf{q})$. We define the minimum value of $\nu_{\rm res}(\mathbf{q})$ as Ω_{mag}. A simple experimentation with the momentum integral shows that Im χ^2 is small at $\Omega<2\Omega_{\rm mag}$, but enhances sharply at $\Omega\geq 2\Omega_{\rm mag}$. In order to illustrate this effect more concretely, we adopt a simple model for the dispersion of the pole. Namely, we set $\nu_{\rm res}(\mathbf{q}) = \Omega_{mag}+\alpha q^2$. Integrating in Eq. (22) over q and substituting the result into (19) we obtain

$$\chi_R(\Omega) = \frac{\Gamma_{tr}^2 a^2}{8\pi\alpha\Omega^2}\log\frac{4\Omega^2_{mag}}{4\Omega^2_{mag}-\Omega^2}. \tag{23}$$

We see that in the two-loop approximation, $\text{Im}\,\chi_R(\Omega)$ undergoes a jump from zero to a finite value at $\Omega = 2\Omega_{mag}$. The real part of the Raman susceptibility $\text{Re}\,\chi_R(\Omega)$ diverges logarithmically at this frequency. Below we verify this result by evaluating (20) numerically.

We next follow the same path as in the normal state and include higher order diagrams (Fig. 3) with the interactions between the two spin fluctuations, i.e., replace the two-loop result $\chi_R = \Gamma^2_{tr}\chi^2(\Omega)$ by

$$\chi_R(\Omega) = \Gamma^2_{tr}\chi_{I-nem}(\Omega) = \Gamma^2_{tr}\frac{\chi^2(\Omega)}{1+2g\chi^2(\Omega)}. \tag{24}$$

Because Re χ^2 diverges upon approaching $2\Omega_{mag}$ from below, Im χ^2 vanishes below $2\Omega_{mag}$, and $g<0$, the full $\text{Im}\chi_R(\Omega)$ has a true pole at some frequency $\Omega=\Omega_{res,1} < 2\Omega_{mag}$.

We now verify the approximation that Γ_{tr} can be taken out of the integral over the bosonic frequency ν. The triangular vertex contains one internal frequency ω and two external ones: Ω, at which we probe the Raman response, and the bosonic frequency μ. For Ω we take the resonance frequency $\Omega_{res,1} < 2\Omega_{mag}$. Typical bosonic frequency $\nu\sim\Omega_{mag}$ and typical ω is Δ. Obviously then, the AL vertex Γ_{tr} is independent on ν if Ω_{mag} is much smaller than Δ, i.e., when internal energy in the AL diagram made out of three fermionic Green's functions is much larger than both external frequencies.

The condition $\Omega_{mag}\ll\Delta$ is satisfied when the inverse magnetic correlation length m_s is small enough because $\Omega_{mag}\propto m_s$ (Ref. [31]). Like we said in the Introduction, in Fe-based materials, where B_{1g} resonance has been observed, the situation is somewhat different: neutron scattering data for $NaFe_{1-x}Co_xAs$ with $x=0.045$ show[32] that $\Omega_{\rm mag}\approx 7$ meV, while $\Delta = 5-5.5meV$ (Ref. [33]), i.e. Δ is somewhat smaller. In this situation, there is no good reason to treat Γ_{tr} as a constant.

In the next Section we analyze another scenario, which is justified in the opposite limit when Ω_{mag} is much larger than Δ.

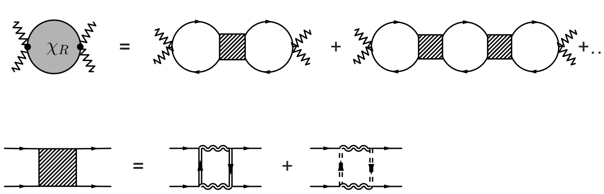

Figure 8. Re-interpretation of series of AL diagrams for χ_R with interactions between spin fluctuations as series consisting of multople particle-hole bubbles with zero momentum and finite frequency transfer (unshaded circles), separated by effective interactions mediated by spin-fluctuations. Each interaction vertex (shaded rectangle) is the convolution of two fermionic and two bosonic propagators. A particular subset of diagrams is shown, with fermions from one of the hole band (solid lines). Double solid and double dashed lines describe fermions from two electron bands.

B. Another interpretation of AL contribution to the B_{1g} Raman response below T_c.

In this Section we look at the second-order AL diagram from Fig. 2 through different lenses. Namely, we abandon the approximation in which Γ_{tr} is treated as a constant and instead use the fact that on both ends incoming and outgoing fermionic momenta are identical (either $\mathbf{k}$ or $\mathbf{p}$), while frequencies differ by Ω, and reinterpret this diagram as consisting of the product of two particle-hole polarization operators at zero transferred momentum and finite frequency, $\Pi_{B_{1g}}(\Omega)$ (the same as in Eq. (2)), separated by magnetically-mediated effective interaction λ_{mag} (see Fig.8). The latter is the convolution of two fermionic and two bosonic propagators. Viewed this way, the two-loop AL diagram has the same structure as the two-loop diagram from RPA series in Eq. (2). Accordingly, λ_{mag} and the bare λ are combined into $\lambda_{eff} = \lambda + \lambda_{mag}$. If the combined λ_{eff} is negative, $1+\lambda_{eff}\Pi_{B_{1g}}(\Omega)$ necessary vanishes at some frequency below 2Δ because Im $\Pi_{B_{1g}}(\Omega)$ vanishes below 2Δ and Re $\Pi_{B_{1g}}(\Omega)$ diverges as $1/\sqrt{4\Delta^2-\Omega^2}$ when $|\Omega|$ approaches 2Δ from below. The vanishing of $1+\lambda_{eff}\Pi_{B_{1g}}(\Omega)$ implies that Raman intensity has an excitonic resonance at $\Omega = \Omega_{res,2}$.

The representation of the two-loop AL diagram from Fig. 2 as $\lambda_{mag}\Pi^2_{B_{1g}}(\Omega)$ with a constant λ_{mag} is again an approximation because the result for the convolution of two fermionic and two bosonic propagators generally depends on external momentum in frequency. The singular behavior of particle-hole polarization bubble $\Pi_{B_{1g}}(\Omega)$ at $\Omega \approx 2\Delta$ comes from internal frequencies near $\pm\Delta$. Internal frequencies in the fermionic-bosonic loop for λ_{mag} are of order Ω_{mag}. If Ω_{mag} is much larger than Δ, a typical internal frequency is much larger than a typical external frequency. The latter can then be sent to zero, in which case λ_{mag} becomes a constant. The frequency $\Omega_{mag} < 2\Delta$ and hence it can be at most twice Δ. But number-wise this may be sufficient to treat λ_{mag} as a constant. The same distinction holds for internal/external momenta, and the result is that, to the same accuracy, λ_{eff} can be evaluated by placing external momenta on the Fermi surface.

We compute λ_{eff} first in the normal state and then in a superconductor, assuming formally that $\Omega_{mag} \gg \Delta$. To simplify calculations, we set $\mu = 0$, i.e., assume that the size of hole/electron pockets is infinitesimally small. The argument is that, if λ_{eff} has a definite sign in this limit, then, by continuity, the sign should remain the same at a small but finite μ.

In the normal state, the coupling λ_{mag} is given by

$$\lambda_{mag} = -g^2_{sf} \int \frac{\mathrm{d}^2\mathbf{q}\mathrm{d}\nu}{(2\pi)^3} G^2(\mathbf{q},\nu)\left(\chi^s(\mathbf{q},\nu)\right)^2 \tag{25}$$

where ν is Matsubara frequency. For definiteness, we take fermions from one of electron bands, i.e., use $G(\mathbf{q},\nu) = 1/(i\nu - q^2/(2m))$. We verified that λ_{mag} does not change if we instead take fermions from the hole band. For the dynamical spin susceptibility we use Landau-overdamped form extended to Matsubara frequencies: $\chi(\mathrm{q},\nu) = 1/(q^2 + m_s^2 + |\nu|/\nu_0)$, where ν_0 is a positive constant.

Substituting the forms of bosonic and fermionic propagators into (25) we obtain

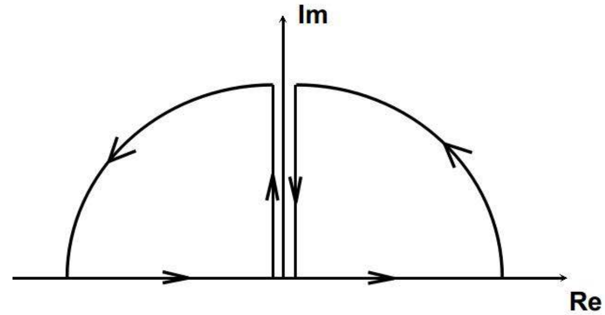

Figure 9. Contour of integration over frequency ν in Eq. 26.

$$\lambda_{mag} = -g^2_{sf}\int \frac{\mathrm{d}^2\mathbf{q}\mathrm{d}\nu}{(2\pi)^3}\frac{1}{(i\nu - \mathbf{q}^2/(2m))^2}\frac{1}{(\mathbf{q}^2+m_s^2+|\nu|/\nu_0)^2}$$
$$= \frac{\nu_0^2 m}{(2\pi)^2}\int_0^\infty \mathrm{d}x \int_{-\infty}^{\infty}\mathrm{d}\nu \frac{1}{(\nu+ix)^2}\frac{1}{(|\nu|+\nu_0 m_s^2+\nu_0 m x)^2}. \tag{26}$$

The double pole in the fermionic Green's function is located at $\nu = -ix$. It is then convenient to evaluate the frequency integral by closing the integration contour over the upper half-plane of complex ν (see Fig. 9). The integrand vanishes at $|\nu| \to \infty$, and if χ^s was an analytic function of ν, λ_{mag} would be zero. But this is not the case because the Landau damping term contains $|\nu| = \sqrt{\nu^2}$, which is non-analytic function of ν along imaginary axis in both half-planes. Choosing the integration contour as shown in Fig. 9 and using $|iz+\epsilon| = iz\,\mathrm{sgn}\,\epsilon$, we obtain after a simple algebra

$$\lambda_{mag} = -ig^2_{sf}\frac{\nu_0^2 m}{(2\pi)^2}\int_0^\infty \mathrm{d}x\int_0^\infty \mathrm{d}z\frac{1}{(z+x)^2}\times$$
$$\left[\frac{1}{(iz+\nu_0 m_s^2+\nu_0 m x)^2} - \frac{1}{(-iz+\nu_0 m_s^2+\nu_0 m x)^2}\right]$$
$$= -\frac{4g^2_{sf}\nu_0^2 m}{(2\pi)^2}\times$$
$$\int_0^\infty \mathrm{d}x\int_0^\infty \mathrm{d}z\frac{z(\nu_0 m_s^2+\nu_0 m x)}{(z+x)^2[z^2+\nu_0^2(m_s^2+mx)^2]^2} \tag{27}$$

The integrand is positive, hence $\lambda_{mag} < 0$. Estimating the integral, we obtain $\lambda_{mag} \propto 1/m_s^4$, i.e., λ_{mag} strongly increases near the magnetic instability.

In the superconducting state, we represent spin-fluctuation propagator by Eq. (18), i.e., by $\chi(\mathrm{q},\nu) = a/(\nu^2+\nu^2_{res}(\mathbf{q}))$, and use $\nu_{res}(\mathbf{q}) = \Omega_{mag} + \alpha q^2$. We assume and then verify that typical ν in the integral for λ_{mag} are of order Ω_{mag}. Because we assume $\Omega_{mag} \gg \Delta$, we can still use normal state Green's functions for fermions Substituting into (25) we obtain

$$\lambda_{mag} =$$
$$- g_{sf}^2 \int \frac{\mathrm{d}^2\mathbf{q}\mathrm{d}\nu}{(2\pi)^3} \frac{1}{(i\nu - \mathbf{q}^2/(2m))^2} \frac{a}{(\nu^2 + (\Omega_{mag} + \alpha q^2)^2)^2}$$
$$= \frac{g_{sf}^2}{4\pi^2} \frac{ma}{\Omega_{mag}^4} \int_0^\infty \mathrm{d}x \int_{-\infty}^{\infty} \mathrm{d}\nu \frac{1}{(\nu + ix)^2} \frac{1}{(\nu^2 + (1+\beta x)^2)^2}. \tag{28}$$

where $\beta = 2m\alpha$ is a dimensionless parameter. The integrand, viewed as a function of ν, contains two double poles in the lower half-plane, at $\nu = -ix$ and at $\nu = -i(1 + \beta x)$, and the double pole in the upper half-plane, at $\nu = i(1 + \beta x)$. The last two double poles come from χ^2. Evaluating the frequency integral by standard means, we obtain after simple algebra that

$$\lambda_{mag} = -\frac{g_{sf}^2}{8\pi} \frac{ma}{\Omega_{mag}^4} \int_0^\infty \mathrm{d}x \frac{3 + x(1 + 3\beta)}{(1 + \beta x)^3(1 + (1 + \beta)x)^3} \tag{29}$$

The integrand is positive for all $x > 0$, hence $\lambda_{mag} < 0$, like in the normal state. Furthermore, because $\Omega_{mag} \propto m_s$, we still have $\lambda_{mag} \propto 1/m_s^4$.

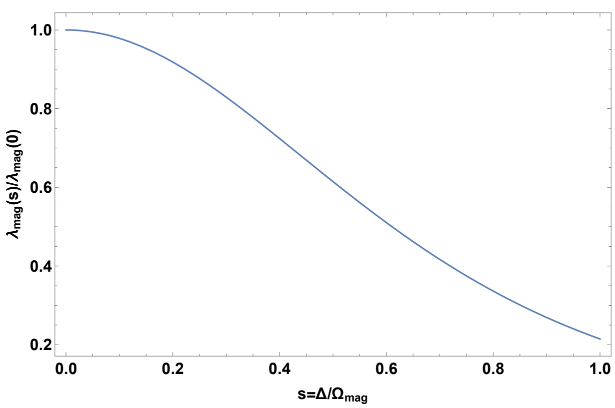

Figure 10. The dependence of the effective spin-mediated 4-fermion interaction $\lambda_{mag}(s)$ on $s = \Delta/\Omega_{mag}$, see Eq. (30). We set $\beta = 1$ for definiteness.

Like we said, the condition $\Omega_{mag} \gg \Delta$ is not realized because $\Omega_{mag} \leq 2\Delta$. To estimate how λ_{mag} changes when Ω_{mag} and Δ become comparable, we use the fact that 2Δ singularity in the particle-hole bubble comes from fermions with frequencies near $\pm\Delta$ and evaluate λ_{mag} in the superconducting state for the case when the frequencies of the two bosonic propagators differ by $\Omega_m = 2\Delta$. The calculation is straightforward, and the result is that λ_{mag} becomes a function of $s = \Delta/\Omega_{mag}$. The dependence on s is given by

$$\lambda_{mag}(s) = -\frac{g_{sf}^2}{8\pi} \frac{ma}{\Omega_{mag}^4} \times$$
$$\int_0^\infty \mathrm{d}x \frac{((1 + (1 + \beta)x)(3 + x(1 + 3\beta)) - s^2}{(1 + \beta x)((1 + \beta x)^2 + s^2)((1 + (1 + \beta)x)^2 + s^2)^2} \tag{30}$$

We plot $\lambda_{mag}(s)$ in Fig. 10. We see that $\lambda_{mag}(s)$ drops when $s = \Delta/\Omega_{mag}$ increases, but the ratio $\lambda_{mag}(s)/\lambda_{mag}(0)$ remains of order one when Δ and Ω_{mag} become comparable.

Combining this last observation with the fact that $\lambda_{mag}(0) \propto 1/m_s^4$, we conclude that for small enough m_s, $|\lambda_{mag}|$ is definitely larger than the bare interaction λ, hence $\lambda_{eff} = \lambda + \lambda_{mag}$ is negative, no matter what is the sign of λ.

One can go a step further and add to the interaction vertex in Fig. 8 (the shaded rectangle) the renormalizations coming from fermions with energies higher than Ω_{mag}. These terms renormalize the convolution of two spin-fluctuation propagators $\chi^2(\Omega)$ into $\chi_{I-nem} = \chi^2/(1 + 2g\chi^2(\Omega))$ and hence add the same denominator to λ_{mag}. As the consequence, λ_{mag} diverges already at the Ising-nematic instability, before m_s vanishes.

By continuity, we assume that λ_{mag} remains negative also for finite hole and electron pockets. Using further RPA form for the Raman intensity, Eq. (2), we obtain that $\chi_R(\Omega)$ has the singularity at $\Omega = \Omega_{res,2} < 2\Delta$, at which $1 + \lambda_{eff}\Pi_{B_{1g}}(\Omega) = 0$.

Finally, we briefly comment on the difference between our analysis and earlier phenomenological consideration of the bi-linear coupling between B_{1g} orbital order parameter $\Delta_{oo} = \sum_k < c_k^\dagger c_k \cos 2\theta_k >$ and $\Delta_1^2 - \Delta_2^2$, where Δ_1 and Δ_2 are spin-fluctuation fields with momenta near Q_1 an Q_2 (Refs.[12,22]) In the microscopic calculation[27] such term appears in the Landau Free energy once we introduce $\Delta_{1,2}$ and Δ_{oo} as order parameter fields, bi-linear in fermions, and perform Hubbard-Stratonovich transformation from fermions to bosonic collective variables. The prefactor A for $\Delta_{oo}(\Delta_1^2 - \Delta_2^2)$ term in the Landau functional is given by the same triangular diagram as AL vertex, and has a finite value (i.e., $A \sim \Gamma_{tr}$). At the first glance, we can identify $\Delta_1^2 - \Delta_2^2$ with the propagator of an Ising-nematic field and obtain the correction to the prefactor for Δ_{oo}^2 in the form $-A^2\chi_{I-nem}$. Because the bare prefactor is $\Pi_{B_{1g}}^{-1} + \lambda$, $\lambda_{eff} = \lambda - A^2\chi_{I-nem}$. At the second glance, however, we note that the Landau functional in terms of Δ_1 and Δ_2 is not the same as Landau functional expressed in terms of the Ising-nematic field. To obtain the latter one has to do second Hubbard-Stratonovich transformation to the composite Ising-nematic bosonic field Δ_{I-nem} and integrate over the primary fields Δ_1 and Δ_2. Only then one can extract the bi-linear coupling between orbital and Ising-nematic order parameters. Another way to see that $A^2\chi_{I-nem}$ with $A \sim \Gamma_{tr}$ is not the correction to λ is to notice that this expression is the full result for the Raman bubble rather than for the effective interaction between fermions from the two particle-hole bubbles.

C. Comparative analysis of the two scenarios

Combining the results of the last two Sections, we see that the resonance in $\chi_R(\Omega)$ holds independent on whether Ω_{mag} is larger or smaller than Δ, but the physics is different in the two cases. When Ω_{mag} is smaller than Δ, the resonance has purely magnetic origin and comes from the pole in χ_{I-nem} at $\Omega = \Omega_{res,1} \leq 2\Omega_{mag}$. For this resonance, the role of fermions is to provide some regular coupling, Γ_{tr}, between incoming and outgoing light and a pair of spin fluctuations with momenta near Q_1 or Q_2. When $\Omega_{mag} > \Delta$, the resonance comes from fermions and is due to singular behavior of particle-hole polarization bubble $\Pi_{B_{1g}}(\Omega)$ at $\Omega = 2\Delta$. The resonance occurs at a frequency $\Omega = \Omega_{res,2} \leq 2\Delta$. Spin fluctuations are again crucial, but now their role is to provide strong attractive interaction between fermions which make particle-hole bubbles.

We treated the two singularities in $\chi_R(\Omega)$ independent on each other chiefly to demonstrate that they come from two different pieces of physics. Such a treatment, however, is justified only if $\Omega_{res,1}$ and $\Omega_{res,2}$ are well separated. In our case, $\Omega_{res,1} \leq 2\Omega_{mag} < 4\Delta$, while $\Omega_{res,2} \leq 2\Delta$. How well $\Omega_{res,1}$ and $\Omega_{res,2}$ are separated then depends on the strength of various interactions and on the value of magnetic correlation length. Like we said, in FeSCs which we analyze Ω_{mag} and Δ are not far from each other. In this case the resonance likely has dual origin. In $NaFe_{1-x}Co_xAs$ with $x = 0.045$, the B_{1g} peak is seen at 7.1 meV, which is below both 2Δ and $2\Omega_{mag}$. This is consistent with the dual origin of the resonance.

D. Numerical evaluation of the AL diagrams

In this Section we present the results of numerical evaluation of AL contributions to B_{1g} Raman intensity below T_c first in the two-loop approximation and then including the interaction between spin fluctuations. We first compute AL vertex assuming that Γ_{tr} can be approximated by a constant and then present the results of the explicit calculation of the two-loop AL diagram for $\chi_R(\Omega)$.

The first step for numerical evaluation of χ_R is to calculate the time-ordered polarization function $\Pi_{s,ij}$ with fermions lines from bands i and j. The bare spin response can be obtained as a time-ordered average of spin operators over a non-interacting ground state. In the FeSCs, the response is largest near the nesting momenta $\mathbf{Q}_x = (\pi, 0)$ or $\mathbf{Q}_y = (0, \pi)$ which connect one hole pocket and one electron pocket. Since we are solely interested in evaluating the function near those momenta we will only consider band combinations of one hole and one electron pocket and drop the band indices from here on. We evaluate the function at momentum $\mathbf{Q}+\mathbf{q}$, where $\mathbf{Q}$ is either $\mathbf{Q}_x$ or $\mathbf{Q}_y$, whichever is appropriate.

For concreteness, we assume parabolic dispersions for the hole and electron pockets of the form $\xi_{\mathbf{k}} = \mu - \frac{k^2}{2m_h}$ and $\xi_{\mathbf{k+Q}} = -\mu + \frac{k_x^2}{2m_x} + \frac{k_y^2}{2m_y}$, respectively. We evaluate all quantities in units of the gap Δ and for numerical parameters we choose $\mu = 2\Delta$, $m_h \approx 0.056\Delta^{-1}$ ($k_F = 0.15\pi/a$), $m_x = m_h/1.27$ and $m_y = m_x/0.3787$. These values approximately fit the bands and Fermi surfaces reported in ARPES measurements[38] of $NaFe_{1-x}Co_xAs$ for $x = 0.05$ (of the two hole bands, we fitted the one with the largest Fermi surface). For numerical convergence we included a finite broadening $\eta = \Delta/100$.

The general behavior of Π_s can be seen in Figs. 11 and 12. The first one shows a frequency sweep of the real part at $\mathbf{q} = 0$ and the divergence at 2Δ is clearly seen. The imaginary part (not shown) vanishes as $\eta \to 0$. This behavior holds unless $\mathbf{q}$ is so large that the normal-state FSs no longer intersect due to the shift. The second plot shows an example of the $\mathbf{q}$ dependence at $\nu = 0$. Although the function is anisotropic due to the eccentricity of the electron Fermi surface, the qualitative behavior is the same regardless of the polar angle. It is particularly important to emphasize that the function decreases monotonically with increasing $|\mathbf{q}|$.

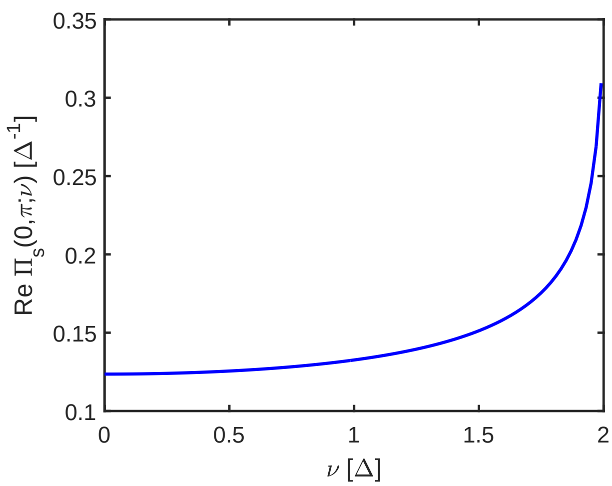

Figure 11. Frequency dependence of the bare spin polarization operator with momentum $(0, \pi)$.

In the numerical analysis, it is easier to deal with the effective interaction in the spin channel U_{eff} rather than the spin susceptibility. In the RPA

$$U_{\text{eff}}(\mathbf{Q}+\mathbf{q}, \nu) = \frac{u}{2} \frac{1}{1 - u\Pi_s(\mathbf{Q}+\mathbf{q}, \nu)}, \tag{31}$$

where $u > 0$ is the bare fermion-fermion interaction ($= U$ in the Hubbard model). The effective interaction is related to the spin susceptibility by $U_{\text{eff}}(\mathbf{Q}+\mathbf{q}, \nu) = (u + u^2\chi^s(\mathbf{Q}+\mathbf{q}, \nu))/2$, so the two functions have the same pole structure and differ only by a constant shift u which near a magnetic instability is small compared to the second term. The $u^2/2$ factor in front of χ^s is the same factor as in (9).

Fig. 13 shows U_{eff} at $\mathbf{q} = 0$ as a function of ν. The real part diverges at the resonance frequency while the imaginary part has a sharp peak which in the limit of $\eta \to 0$ becomes a δ function. For the numerical calculations we have set $u \approx 7.9\Delta$ which determines $\Omega_{\text{mag}} \approx 0.6\Delta$.

Now we are ready to evaluate the Raman response (20). By using the spectral representation, the imaginary part

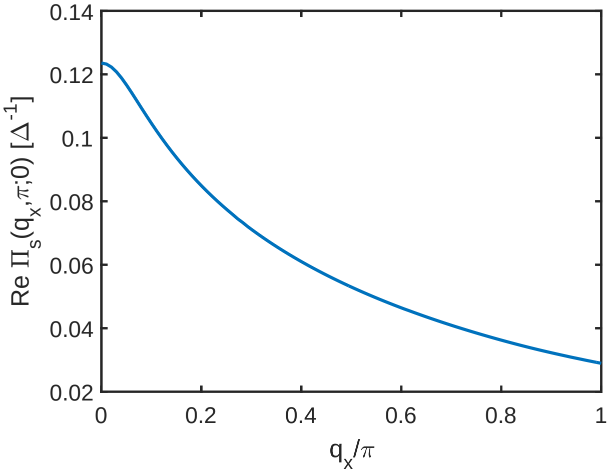

Figure 12. Momentum dependence of the static spin polarization operator with momentum near $(0,\pi)$. We have chosen momenta to be $\mathbf{q}+(0,\pi)$. The dependence on q_x is shown. The dependence on the polar angle of $\mathbf{q}$ is non-zero but rather weak.

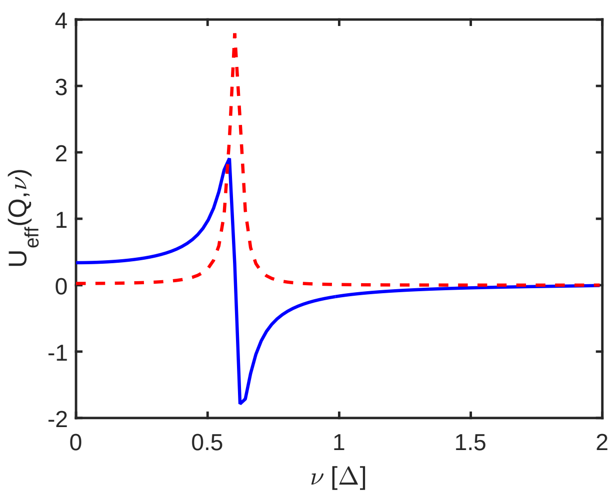

Figure 13. Frequency dependence of the real (solid blue line) and imaginary (dashed red line) parts of the effective interaction (in arbitrary units).

of the response function can be equivalently calculated as

$$\operatorname{Im}\chi_R(\Omega) \propto \int \frac{\mathrm{d}^2\mathbf{q}}{(2\pi)^2}\int_0^{\Omega}\frac{\mathrm{d}\nu}{\pi}\operatorname{Im}U_{eff}(\mathbf{Q}+\mathbf{q},\nu) \times \operatorname{Im}U_{eff}(\mathbf{Q}+\mathbf{q},\nu-\Omega). \quad (32)$$

The advantage of this form is that it only requires knowledge of the function in a finite range of ν. The real part can then be calculated by using the KK transformation.

Because $\operatorname{Im}U_{\text{eff}}(\mathbf{Q}+\mathbf{q},\nu)$ is peaked at the resonant frequencies corresponding to each momentum $\mathbf{q}$, $\operatorname{Im}\chi_R(\Omega)$ can be seen as a convolution of many of these peaks. The result of the computation is shown in Fig. 14. We see that the imaginary part starts small and undergoes a jump at $\nu \approx 1.2\Delta = 2\Omega_{\text{mag}}$, (compare to Fig. 13). Its value at higher frequencies comes from contributions from $\mathbf{q}\neq 0$, corresponding to excitons of higher energies. This jump is not sharp in the numerical calculations because of the finite value of η in (17).

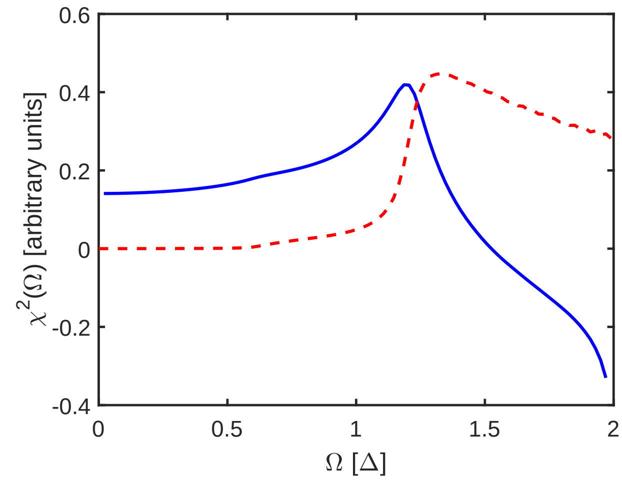

Figure 14. Contribution to Raman response from spin fluctuations. The solid blue and dashed red lines indicate the real and imaginary parts, respectively.

We next consider the effect of the finite state interaction, i.e., include higher order diagrams (Fig. 3) with the interactions between the two spin fluctuations. In the approximation where the interactions between pairs of spin fluctuations with momenta near Q_1 and/or Q_2 can be treated as constants, we use Eq. (24) We plot the RPA form of $\chi_R(\Omega)$ in Fig. 15. We clearly see that $\operatorname{Im}\chi_R^0(\Omega)$ has a sharp peak at a frequency $\Omega < 2\Omega_{\text{mag}}$, which is below 2Δ.

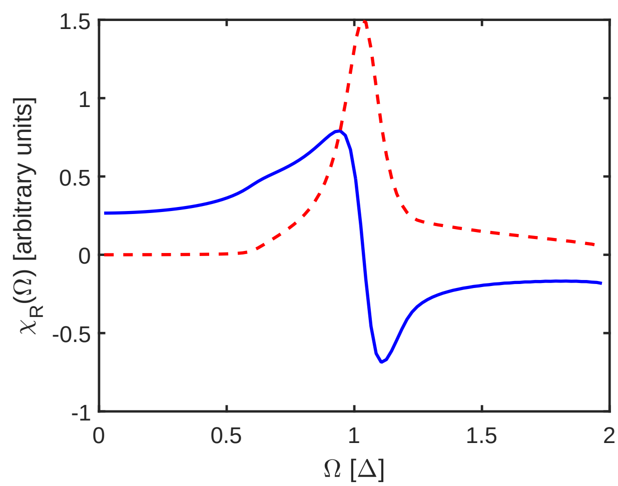

Figure 15. The full Raman susceptibility, which includes interactions between spin fluctuations. The solid blue line indicates the real part and the dashed red line the imaginary part of the function. We set $g = 1.66$.

V. TRIANGULAR FERMION LOOP AND SYMMETRY CHANNELS

So far, we have neglected the details of the Raman vertex Γ_{tr} and thus the analysis above applies equally to all symmetry channels. We remind that in the experiments the resonance has been observed in the B_{1g} channel in the 1-Fe unit cell, but no resonance has been observed in the B_{2g} or A_{1g} channels. To address the origin of the difference between Raman scattering in different symmetry channels, we consider the symmetry properties of the function $\Gamma_{tr}(\mathbf{q},\nu)$, defined in (7).

First we focus on the bare Raman vertices. The original Raman vertex $\gamma_i(\mathbf{k})$ between incoming and outgoing light and incoming and outgoing fermions from band i belongs to the irreducible representations of the point group D_{4h}. As a reminder, we point out that in the B_{1g} and B_{2g} representations, the function $\gamma_i(\mathbf{k})$ transforms under the point group operations as $k_x^2-k_y^2$ and k_xk_y, respectively, while in the A_{1g} representation $\gamma_i(\mathbf{k})$ is invariant under the point group operations. We will consider each of these channels separately.

In the B_{1g} channel, the Raman response is directly coupled to nematic orbital fluctuations and in the orbital basis we can define it as

$$\chi_R(\Omega) = -i\int \mathrm{d}te^{i\Omega t}\langle T\rho_n(t)\rho_n(0)\rangle, \qquad (33)$$

where the nematic "density" operator is defined as $\rho_n = \frac{1}{\sqrt{N}}\sum_{\mathbf{k},\sigma}\left[a^\dagger_{\mathbf{k}\sigma}a_{\mathbf{k}\sigma} - b^\dagger_{\mathbf{k}\sigma}b_{\mathbf{k}\sigma}\right]$. In this notation, the fermion operators a and b correspond to the d_{xz} and d_{yz} orbitals, respectively.

The transformation from the orbital to the band basis in the case of the hole pockets can be approximated by[47]

$$\begin{aligned}\alpha_{\mathbf{k}\sigma} &= \cos\theta_{\mathbf{k}}a_{\mathbf{k}\sigma} - \sin\theta_{\mathbf{k}}b_{\mathbf{k}\sigma},\\ \beta_{\mathbf{k}\sigma} &= \sin\theta_{\mathbf{k}}a_{\mathbf{k}\sigma} + \cos\theta_{\mathbf{k}}b_{\mathbf{k}\sigma},\end{aligned} \qquad (34)$$

where α and β are denote the hole bands and θ is the angle along the Fermi surface.

The contribution to the nematic density operator from fermions from the hole bands then becomes

$$\begin{aligned}\rho_n =& \sum_{\mathbf{k}}(\alpha^\dagger_{\mathbf{k}\sigma}\alpha_{\mathbf{k}\sigma} - \beta^\dagger_{\mathbf{k}\sigma}\beta_{\mathbf{k}\sigma})\cos 2\theta_{\mathbf{k}}\\ &+\sum_{\mathbf{k}}(\alpha^\dagger_{\mathbf{k}\sigma}\beta_{\mathbf{k}\sigma} + \beta^\dagger_{\mathbf{k}\sigma}\alpha_{\mathbf{k}\sigma})\sin 2\theta_{\mathbf{k}}.\end{aligned} \qquad (35)$$

The second term can be neglected at low energies because it couples fermions from different Fermi surfaces, which do not cross. Substituting into (33) we find that the vertex function for holes $\gamma_i(\mathbf{k})$ in the B_{1g} channel is $\cos(2\theta_{\mathbf{k}})$ and has opposite signs for the two hole bands. For electron pockets, the situation is more simple since each electron pocket only has contributions from the d_{zx} or d_{yz} orbital, but no from both. The transformation from the orbital to the band basis is trivial and we find that $\gamma_i(\mathbf{k}) = \pm 1$, where the plus sign is for the electrons from the pocket near $\mathbf{Q}_1 = (\pi, 0)$ and the minus sign for electrons near $\mathbf{Q}_2 = (0,\pi)$.

Diagram	γ_{B1g}	γ_{B2g}	γ_{A1g}^{++}	γ_{A1g}^{+-}
(a)	$\cos 2\theta$	$\sin 2\theta$	1	1
(b)	$-\cos 2\theta$	$-\sin 2\theta$	1	1
(c)	1	0	1	-1
(d)	1	0	1	-1
(e)	$\cos 2\theta$	$\sin 2\theta$	1	1
(f)	$-\cos 2\theta$	$-\sin 2\theta$	1	1
(g)	-1	0	1	-1
(h)	-1	0	1	-1

Table I. Symmetry factors for Raman vertices in different symmetry channels. We include two different representations of A_{1g} symmetry: One where the sign changes between hole and electron pockets, and one in which it does not (see text).

For the B_{2g} channel one can define a different density operator $\rho_{B2g} = \frac{1}{\sqrt{N}}\sum_{\mathbf{k},\sigma}\left[a^\dagger_{\mathbf{k}\sigma}b_{\mathbf{k}\sigma} + b^\dagger_{\mathbf{k}\sigma}a_{\mathbf{k}\sigma}\right]$. Then using again the transformation (34) one finds that for hole bands the appropriate B_{2g} symmetry factor is $\gamma_i(\mathbf{k}) = \pm\sin(2\theta_{\mathbf{k}})$. For electron bands the symmetry factor is instead $\gamma_i(\mathbf{k}) = 0$ since the electron bands do not cross.

Finally, the Raman vertex in the A_{1g} channel is a constant along hole or electron pockets. In general, there are two possibilities: The symmetry factor can have the same sign for the coupling of light to electrons and holes, or change sign when switching between electrons and holes. In order to consider both possibilities we define two separate functions γ_{A1g}^{++} and γ_{A1g}^{+-}, referring to the cases with equal and opposite signs, respectively.

An additional effect of the orbital to band transformation (34) is that the factors of sine and cosine contribute extra angular dependence to the momentum integration in Λ. This is summarized graphically in Fig. 16, where we list the different band combinations with the appropriate signs and angular dependences. The symmetry factor $\gamma(\mathbf{k})$ for each diagram in different symmetry channels is given in Table I. The first four diagrams are for the interaction between light and spin fluctuations with momentum near $\mathbf{Q}_x$ and the other four are for momentum near $\mathbf{Q}_y$. The total contribution to Λ in each case is given by the sum of the four diagrams. The angular dependencies listed in the figure are for a model with only intra-orbital Hubbard interaction.

The result of the momentum integration is different depending on the symmetry channel. For simplicity in the evaluation of the integral, we consider identical circular Fermi surfaces in all bands and evaluate the bare triangular vertices $\Gamma^0_{tr}(\mathbf{q},\nu)$ in various geometries at $\mathbf{q}=0$. This particular value of $\mathbf{q}$ is important because the enhancement in $\chi^2(\Omega)$ at $\Omega = \Omega_{\rm mag}$ comes primarily from momenta near $\mathbf{q}=0$. Considering only the angular part

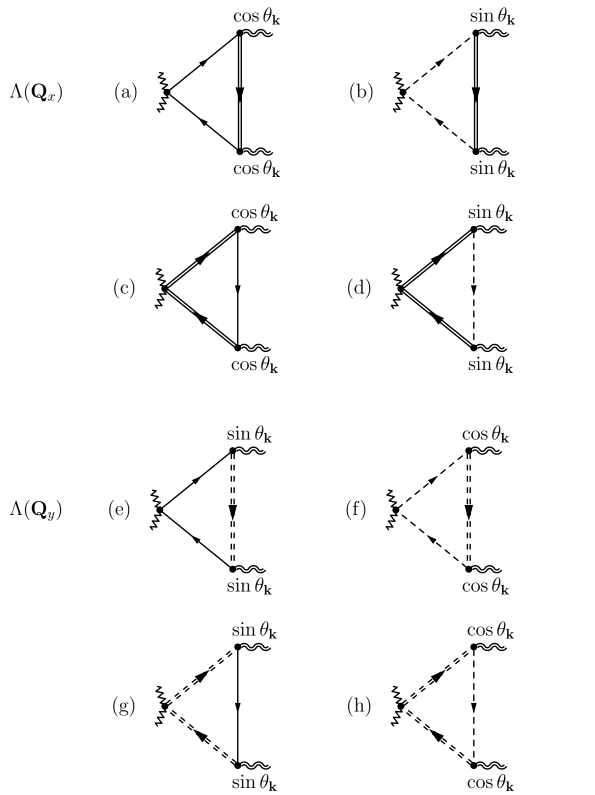

Figure 16. Contributions to the triangular fermion loop from different bands. The single solid and dashed lines represent the hole bands α and β, respectively, while the double solid and dashed lines represent electron bands centered at momentum $\mathbf{Q}_x$ and $\mathbf{Q}_y$, respectively. The factors of $\cos\theta$ and $\sin\theta$ arise from the transformation from the orbital to the band basis (see text).

of the integration, we find that

$$\Gamma_{tr}^{0,B_{1g}} \propto \int \mathrm{d}\theta_{\mathbf{k}} (\cos 2\theta_{\mathbf{k}} \cos 2\theta_{\mathbf{k}} - 1) \neq 0 \tag{36}$$

$$\Gamma_{tr}^{0,B_{2g}} \propto \int \mathrm{d}\theta_{\mathbf{k}} \sin 2\theta_{\mathbf{k}} \cos 2\theta_{\mathbf{k}} = 0 \tag{37}$$

$$\Gamma_{tr}^{0,++} \propto \int \mathrm{d}\theta_{\mathbf{k}} (1-1) = 0 \tag{38}$$

$$\Gamma_{tr}^{0,+-} \propto \int \mathrm{d}\theta_{\mathbf{k}} (1+1) \neq 0 \tag{39}$$

where, we remind, $\Gamma_{tr}^{0,++}$ and $\Gamma_{tr}^{0,+-}$ are two different triangular vertices in A_{1g} channel. We see that $\Gamma_{tr}^{0,B_{2g}}$ and $\Gamma_{tr}^{0,++}$ vanish, i.e., there is no enhancement of the Raman intensity in the B_{2g} or A_{1g}^{++} channels, in agreement with the data.

One fine point in the calculation is that the contribution from diagrams with electron bands at the vertex has an additional minus sign compared to diagrams with hole bands at the vertex (for example, compare diagrams (c) and (d) with (a) and (b)). This is not a symmetry factor but instead comes from the opposite signs between the hole and electron band dispersions and can be obtained after performing the frequency integration in the Fermion loop. In the sign-preserving A_{1g} channel this leads to a complete cancellation while in the B_{1g} channel it is only partial since, e.g., (a) and (b) contribute a factor of $\cos 2\theta$ while (c) and (d) contribute a factor of $-\frac{1}{2}\cos 2\theta$.

To summarize, we have shown so far that the bare vertices for the B_{2g} and sign-preserving A_{1g} channels vanish and thus cannot lead to resonances. The bare vertices in B_{1g} and sign-changing A_{1g} channels are non-zero. Note that the Raman response in sign-changing A_{1g} channel is not screened out by long-range component of Coulomb interaction[3,4]. The response in the sign-preserving A_{1g} channel is screened[14–16], but in our case it vanishes anyway.

The next step is to include interactions between the spin fluctuations and calculate the renormalized vertices $\Gamma_{tr}^{B_{1g}}$ and Γ_{tr}^{+-}.

For this we first introduce vertices $\Gamma_{tr,1}$ and $\Gamma_{tr,2}$, which couple light to spin fluctuations with momentum near $\mathbf{Q}_1$ and $\mathbf{Q}_2$, respectively. The vertices in B_{1g} and A_{1g} channels are related to $\Gamma_{tr,1}$ and $\Gamma_{tr,2}$ as

$$\Gamma_{tr,1} = \Gamma_{tr}^{B_{1g}} + \Gamma_{tr}^{+-}, \quad \Gamma_{tr,2} = \Gamma_{tr}^{+-} - \Gamma_{tr}^{B_{1g}} \tag{40}$$

We then follow Ref. [27] and model the interaction between spin fluctuations as given by the effective action

$$S_{\mathrm{eff}} = r_0(\Delta_1^2 + \Delta_2^2) + \frac{\kappa}{2}(\Delta_1^2 + \Delta_2^2)^2 + \frac{g}{2}(\Delta_1^2 - \Delta_2^2)^2, \tag{41}$$

where Δ_1 and Δ_2 are three-component spin fluctuation fields, respectively, in which each component corresponds to a direction in real space. The 1 and 2 subscripts distinguish between fluctuations near $\mathbf{Q}_1$ and $\mathbf{Q}_2$. This effective action can obtained by introducing Hubbard-Stratonovich fields and then integrating out fermions. The result is[27] that $\kappa > 0$, but g is negative, at least at small dopings.

The bare vertices $\Gamma_{tr,1}^0$ and $\Gamma_{tr,2}^0$ are given by the sum of diagrams (a)-(d) and (e)-(h), respectively. In the ladder approximation, the coupled equations for the renormalized vertices $\Gamma_{tr,1}$ and $\Gamma_{tr,2}$ are given by

$$\Gamma_{tr,1} = \Gamma_{tr,1}^0 - (\kappa+g)\Gamma_{tr,1}\chi^2 - (\kappa-g)\Gamma_{tr,2}\chi^2, \tag{42}$$

$$\Gamma_{tr,2} = \Gamma_{tr,2}^0 - (\kappa+g)\Gamma_{tr,2}\chi^2 - (\kappa-g)\Gamma_{tr,1}\chi^2, \tag{43}$$

where we remind that χ^2 is the shorthand notation for $\int \frac{\mathrm{d}^2\mathbf{q}\mathrm{d}\nu}{(2\pi)^3}\chi^{\mathrm{s}}(\mathbf{Q}+\mathbf{q},\nu)\chi^{\mathrm{s}}(\mathbf{Q}+\mathbf{q},\nu+\Omega)$. In this expression we do not distinguish between $\mathbf{Q}_1$ and $\mathbf{Q}_2$ because by symmetry the result of the integration is the same.

These coupled equations can be solved in terms of $\Gamma_{tr}^{B_{1g}}$

and Γ_{tr}^{+-}:

$$\Gamma_{tr}^{+-} = \frac{\Gamma_{tr}^{0,+-}}{1+2\kappa\chi^2}, \tag{44}$$

$$\Gamma_{tr}^{B_{1g}} = \frac{\Gamma_{tr}^{0,B_{1g}}}{1+2g\chi^2}. \tag{45}$$

The renormalized Raman susceptibility is then given by

$$\chi_R^{B_{1g}} = \frac{(\Gamma_{tr}^{0,B_{1g}})^2\chi^2}{1+2g\chi^2}, \tag{46}$$

$$\chi_R^{A1g,+-} = \frac{(\Gamma_{tr}^{0,+-})^2\chi^2}{1+2\kappa\chi^2}. \tag{47}$$

Since $\kappa > 0$ and $g < 0$, only the B_{1g} channel has a resonance, which is consistent with the data. There is no resonance-type enhancement from the coupling to spin fluctuations, regardless of whether the sign-preserving or sign-changing representation is involved. We note in passing that there is a different enhancement of the Raman intensity in the A_{1g} channel in s^{+-} superconductors due to a direct process in which a light generates a ladder series of particle-hole pairs.[3]

We also note that the downward renormalization of Γ_{tr}^{+-} by $1/(1+2\kappa\chi^2)$ also strongly reduces the temperature dependence of the A_{1g} Raman intensity in the normal state. Indeed, explicit calculation shows[27] that $\kappa \sim 1/T^2$. Following the considerations of Sec. III, we find that in the normal state

$$\chi_R^{A1g}(T) \sim \frac{(m_s)^{-2}}{T+T_1}, \tag{48}$$

where $T_1 \gg T_0$ because $\kappa \gg |g|$. This implies that at $T \geq T_0$, $\chi_R^{A1g}(T)$ is nearly flat.

VI. CONCLUSIONS

In this work we argued that the coupling of the Raman vertex to pairs of magnetic fluctuations via the AL process can explain the $1/(T-T_0)$ behavior of B_{1g} Raman intensity in the normal state of $NaFe_{1-x}Co_xAs$, $EuFe_2As_2$, $SrFe_2As_2$, and $Ba(Fe_{1-x}Co_x)_2As_2$ and the development of the resonance below T_c, observed in $NaFe_{1-x}Co_xAs$ and $Ba(Fe_{1-x}Co_x)_2As_2$.

We considered AL process in which light couples to a particle-hole pair which then gets converted into a pair of spin fluctuations with momenta near $Q_1 = (\pi, 0)$ and $Q_2 = (0, \pi)$. We analyzed magnetically-mediated Raman intensity both analytically and numerically, first at the leading two-loop order and then included interactions between pairs of magnetic fluctuations. We demonstrated explicitly that the full Raman intensity in the B_{1g} channel can be viewed as the result of the coupling of light to Ising-nematic susceptibility via Aslamazov-Larkin process. We argued that the $1/(T-T_0)$ temperature dependence in the normal state is the combination of the temperature dependencies of the Aslamazov-Larkin vertex and of Ising-nematic susceptibility. We further argued that the resonance in the B_{1g} channel below T_c emerges because of two effects. One is the development of a pole in the fully renormalized Ising-nematic susceptibility. The pole occurs at a frequency $\Omega_{res,1} < 2\Omega_{mag}$, where Ω_{mag} is the minimal frequency of a dispersing spin resonance at momenta near $Q_{1,2}$ in an s^{+-} superconductor. Another effect is that spin fluctuations generate attractive interactions between low-energy fermions, which constitute particle-hole bubbles with zero momentum transfer. An attractive interaction between such fermions combined with the fact that in an s-wave superconductor a particle-hole bubble at zero momentum transfer is singular at 2Δ gives rise to an excitonic resonance at $\Omega_{res,2} < 2\Delta$. In FeSCs $\Omega_{res,1}$ and $\Omega_{res,2}$ are not far from each other, and the observed strong peak in B_{1g} Raman intensity below T_c is likely the mixture of both effects.

We acknowledge with thanks conversations with G. Blumberg, Y. Gallais, R. Hackl, R. Fernandes, M. Khodas, H. Kontani, I. Paul, A. Sacuto, J. Schmalian, V. Thorsmølle, and R. Xing. The work is supported by the DOE grant DE-SC0014402.

Appendix A: Orbital fluctuations

In this Appendix we consider the coupling of the Raman response to orbital fluctuations in detail and show that the interaction in the d-wave channel is repulsive and cannot lead to the observed resonance.

As explained in the introduction, the electronic structure of $NaFe_{1-x}Co_xAs$ and $Ba(Fe_{1-x}Co_x)_2As_2$ consists of four bands that cross the Fermi energy. We will refer to the two hole bands centered at $(0,0)$ as α and β and to the electron bands centered at $(\pi, 0)$ and $(0, \pi)$ as η and δ, respectively. We organize our analysis in the language of vertex renormalization. We start with a set of bare Raman vertices $\gamma_i(\mathbf{k})$ with both external fermion lines belonging to the i-th band, then dress each vertex with interactions to obtain the full vertex $\Gamma_i(\mathbf{k})$. Here the index runs over the set of bands $\{\alpha, \beta, \eta, \delta\}$. Since we are interested in computing the Raman response in the limit of vanishingly small external momentum, we do not consider vertices with external fermion lines from two different bands since in the absence of band crossings there will be no low energy contribution from these vertices.

For simplicity we study a model consisting of only d_{xz} and d_{yz} orbitals. Since the remaining d_{xy} orbital has A_{1g} symmetry it cannot directly contribute to the Raman response in the B_{1g} channel. The transformation between the band and orbital basis for the hole pockets was given in (34). For the electron pockets we will simply set $\eta_{\mathbf{k}+\mathbf{Q}_x} = a_{\mathbf{k}+\mathbf{Q}_x}$ and $\delta_{\mathbf{k}+\mathbf{Q}_y} = b_{\mathbf{k}+\mathbf{Q}_y}$. Following the reasoning in section V, the bare B_{1g} Raman vertex is given by $\gamma_i(\mathbf{k}) = \{\cos 2\theta_{\mathbf{k}}, -\cos 2\theta_{\mathbf{k}}, 1, -1\}_i$. The alternating signs reflect the difference between d_{xz} and d_{yz} contributions.

For our perturbative analysis, we assume that the short-range intra-orbital repulsion is the dominant interaction. Thus, the interaction Hamiltonian in the orbital basis is given by

$$\mathcal{H}_I = U \sum_{\mathbf{q}} \left[\rho_{xz}(\mathbf{q})\rho_{xz}(-\mathbf{q}) + \rho_{yz}(\mathbf{q})\rho_{yz}(-\mathbf{q})\right], \quad \text{(A1)}$$

where $\rho_{xz}(\mathbf{q}) = \frac{1}{\sqrt{N}} \sum_{\mathbf{k},\sigma} a^\dagger_{\mathbf{k}+\mathbf{q}\sigma} a_{\mathbf{k}\sigma}$ and $\rho_{yz}(\mathbf{q}) = \frac{1}{\sqrt{N}} \sum_{\mathbf{k},\sigma} b^\dagger_{\mathbf{k}+\mathbf{q}\sigma} b_{\mathbf{k}\sigma}$ are the density operators of the d_{xz} and d_{yz} orbitals, respectively.

Our diagrammatic analysis is summarized in Figs. 17 and 18. For notational convenience we define auxiliary functions $\tilde{\Gamma}_i(\mathbf{k})$ and $ga\tilde{m}ma_i(\mathbf{k})$ such that $\Gamma_i = \{\tilde{\Gamma}_\alpha \cos 2\theta_{\mathbf{k}}, \tilde{\Gamma}_\beta \cos 2\theta_{\mathbf{k}}, \tilde{\Gamma}_\eta, \tilde{\Gamma}_\delta\}_i$ and a similar expression for γ_i. The set of coupled equations for the Raman vertices can be written in matrix form as

$$\tilde{\mathbf{\Gamma}} = \tilde{\gamma} - \mathbf{V}\mathbf{\Pi}\tilde{\gamma}, \quad \text{(A2)}$$

where $\mathbf{V}$ and $\mathbf{\Pi}$ are interaction and polarization matrices, respectively, given by

$$\mathbf{V} = \frac{U}{2} \begin{pmatrix} 1 & -1 & 1 & -1 \\ -1 & 1 & -1 & 1 \\ 1 & -1 & 2 & 0 \\ -1 & 1 & 0 & 2 \end{pmatrix} \quad \text{(A3)}$$

$$\mathbf{\Pi} = \begin{pmatrix} \Pi_\alpha(0,\Omega) & 0 & 0 & 0 \\ 0 & \Pi_\beta(0,\Omega) & 0 & 0 \\ 0 & 0 & \Pi_\eta(0,\Omega) & 0 \\ 0 & 0 & 0 & \Pi_\delta(0,\Omega) \end{pmatrix} \quad \text{(A4)}$$

In this notation, the polarization functions are defined as

$$\Pi_i(0,\Omega) = i \int \frac{\mathrm{d}^2k\mathrm{d}\nu}{(2\pi)^3} s_i(\mathbf{k}) \left[G_i(\mathbf{k},\nu+\Omega)G_i(\mathbf{k},\nu) - F_i(\mathbf{k},\nu+\Omega)F_i(\mathbf{k},\nu)\right], \quad \text{(A5)}$$

where G_i and F_i are normal and anomalous Green's functions for band i, respectively, and $s_i(\mathbf{k}) = \{\cos^2(2\theta_{\mathbf{k}}), \cos^2(2\theta_{\mathbf{k}}), 1, 1\}_i$. We note that by symmetry $\Pi_\eta(0,\Omega) = \Pi_\delta(0,\Omega)$. In this definition, the real part of each function is positive.

The solution to (A2) is easily obtained as $\tilde{\mathbf{\Gamma}} = (\mathbb{I} + \mathbf{V}\mathbf{\Pi})^{-1}\tilde{\gamma}$, where $\mathbb{I}$ is the identity matrix. After evaluation of the matrix multiplication we find that the full vertex is given by

$$\Gamma_i = \left[1 + \frac{U}{2}\sum_j \Pi_j(0,\Omega)\right]^{-1} \gamma_i \quad \text{(A6)}$$

and the full response function takes the simple form

$$\chi_R(\Omega) = \frac{2\sum_i \Pi_i(0,\Omega)}{1 + \lambda \sum_j \Pi_j(0,\Omega)}. \quad \text{(A7)}$$

where $\lambda = U/2 > 0$. This is the same formula as Eq. (2) (with $\Pi_{B_{1g}}(\Omega) = \sum_j \Pi_j(0,\Omega)$). Obviously, for $\lambda > 0$ the Raman susceptibility $\chi_R(\Omega)$ contains no poles and thus orbital fluctuations alone cannot explain the observed resonance in $\chi_R(\Omega)$.

[1] G. R. Boyd, T. P. Devereaux, P. J. Hirschfeld, V. Mishra, and D. J. Scalapino Phys. Rev. B 79, 174521 (2009); G. R. Boyd, P. J. Hirschfeld, and T. P. Devereaux Phys. Rev. B 82, 134506 (2010).

[2] B. Valenzuela, M. J. Caldern, G. Len, and E. Bascones Phys. Rev. B 87, 075136 (2013).

[3] A. V. Chubukov, I. Eremin, and M. M. Korshunov Phys. Rev. B 79, 220501(R) (2009).

[4] C. Sauer and G. Blumberg, Phys. Rev. B **82**, 014525 (2010).

[5] D. J. Scalapino and T. P. Devereaux Phys. Rev. B 80, 140512(R) (2009).

[6] S. Sugai, Y. Mizuno, K. Kiho, M. Nakajima, C. H. Lee, A. Iyo, H. Eisaki, and S. Uchida Phys. Rev. B 82, 140504(R) (2010); ibid 83, 019903 (2011).

[7] I. I. Mazin, T. P. Devereaux, J. G. Analytis, Jiun-Haw Chu, I. R. Fisher, B. Muschler, and R. Hackl, Phys. Rev. B 82, 180502(R) (2010).

[8] F. Kretzschmar, B. Muschler, T. Bhm, A. Baum, R. Hackl, Hai-Hu Wen, V. Tsurkan, J. Deisenhofer, and A. Loidl, Phys. Rev. Lett. 110, 187002 (2013).

[9] V. K. Thorsmølle, M. Khodas, Z. P. Yin, Chenglin Zhang, S. V. Carr, Pengcheng Dai, and G. Blumberg, arXiv:1410.6456.

[10] W.-L. Zhang, P. Richard, H. Ding, Athena S. Sefat, J. Gillett, Suchitra E. Sebastian, M. Khodas, and G. Blumberg, arXiv:1410.6452.

[11] B. Muschler, W. Prestel, R. Hackl, T. P. Devereaux, J. G. Analytis, Jiun-Haw Chu, and I. R. Fisher, Phys. Rev. B **80**, 180510 (2009).

[12] Y. Gallais, R. M. Fernandes, I. Paul, L. Chauvière, Y.-X. Yang, M.-A. Méasson, M. Cazayous, A. Sacuto, D. Colson, and A. Forget, Phys. Rev. Lett. **111**, 267001 (2013).

[13] see, e.g., S. Graser, T. A. Maier, P. J. Hirschfeld, and D. J. Scalapino, New J. Phys. 11, 025016 (2009).

[14] M. V. Klein and S. B. Dierker, Phys. Rev. B 29, 4976 (1984).

[15] T. P. Devereaux and R. Hackl, Reviews of Modern Physics,

vol. 79, 175 (2007) and references therein.
[16] T. Strohm and M. Cardona, Phys. Rev. B **55**, 12725 (1997).
[17] S.L. Cooper and M.V.Klein, Comments Condens. Matter Phys. **15**, 99 (1990); R.R.P.Singh, Comments Condens. Matter Phys. **15**, 241 (1991).
[18] R.M. Fernandes, A.V. Chubukov, and J. Schmalian, Nat. Phys. 10, 97 (2014).
[19] Y. Gallais and I. Paul, arXiv:1508.01319.
[20] H. Yamase and R. Zeyher Phys. Rev. B 88, 125120 (2013); New J. Phys. **17**, 073030 (2015).
[21] G. Blumberg, private communication.
[22] Y. Gallais, I. Paul, L. Chauviére, and J. Schmalian, arXiv:1504.04570.
[23] M. Eschrig, Adv. Phys. **55**, 47 (2006).
[24] Y. Yamakawa, S. Onari, and H. Kontani, arXiv:1509.01161.
[25] A.V. Chubukov, D. Efremov, I. Eremin, Phys. Rev. B 78, 134512 (2008); A.V. Chubukov, Phys. C 469, 640 (2009).
[26] A. F. Kemper, T. A. Maier, S. Graser, H.-P. Cheng, P. J. Hirschfeld, and D. J. Scalapino, New J. Phys. **12**, 073030 (2010).
[27] R. M. Fernandes, A. V. Chubukov, J. Knolle, I. Eremin, and J. Schmalian, Phys. Rev. B **85**, 024534 (2012).
[28] S. Caprara, C. Di Castro, M. Grilli, and D. Suppa Phys. Rev. Lett. **95**, 117004 (2005). See also Hiroshi Kontani, Tetsuro Saito, and Seiichiro Onari Phys. Rev. B **84**, 024528 (2011).
[29] U. Karahasanovic, F. Kretzschmar, T. Bhm, R. Hackl, I. Paul, Y. Gallais, and J. Schmalian, Phys. Rev. B **92**, 075134 (2015).
[30] M. Khodas and A. Levchenko, Phys. Rev. B **91**, 235119 (2015).
[31] Ar. Abanov and A.V. Chubukov, Phys. Rev. Lett. **83**, 1652 (1999).
[32] Chenglin Zhang, H.-F. Li, Yu Song, Yixi Su, Guotai Tan, Tucker Netherton, Caleb Redding, Scott V. Carr, Oleg Sobolev, Astrid Schneidewind, Enrico Faulhaber, L. W. Harriger, Shiliang Li, Xingye Lu, Dao-Xin Yao, Tanmoy Das, A. V. Balatsky, Th. Brckel, J. W. Lynn, and Pengcheng Dai, Phys. Rev. B **88**, 064504 (2013).
[33] Q.Q. Ge *et al*, Phys. Rev. X **3**, 011020 (2013).
[34] R. M. Fernandes, L. H. VanBebber, S. Bhattacharya, P. Chandra, V. Keppens, D. Mandrus, M. A. McGuire, B. C. Sales, A. S. Sefat, and J. Schmalian, Phys. Rev. Lett. **105**, 157003; R.M. Fernandes and J. Schmalian, Supercond. Sci. Technol. 25, 084005 (2012).
[35] Y. Zhang, C. He, Z. R. Ye, J. Jiang, F. Chen, M. Xu, Q. Q. Ge, B. P. Xie, J. Wei, M. Aeschlimann, X. Y. Cui, M. Shi, J. P. Hu, and D. L. Feng, Phys.Rev.B **85**, 085121 (2012).
[36] Ge, Q. Q., Z. R. Ye, M. Xu, Y. Zhang, J. Jiang, B. P. Xie, Y. Song, C. L. Zhang, Pengcheng Dai, and D. L. Feng, Phys. Rev. X **3**, 011020 (2013).
[37] S. T. Cui, S. Y. Zhu, A. F. Wang, S. Kong, S. L. Ju, X. G. Luo, X. H. Chen, G. B. Zhang, and Z. Sun, Phys. Rev. B **86**, 155143 (2012).
[38] Z.-H. Liu, P. Richard, K. Nakayama, G.-F. Chen, S. Dong, J.-B. He, D.-M. Wang, T.-L. Xia, K. Umezawa, T. Kawahara, S. Souma, T. Sato, T. Takahashi, T. Qian, Yaobo Huang, Nan Xu, Yingbo Shi, H. Ding, and S.-C. Wang, Phys. Rev. B **84**, 064519 (2011).
[39] I. Paul, Phys. Rev. B **90**, 115102 (2014).
[40] A.V. Chubukov, Ann. Rev. Condens. Matter Phys. 3, 57 1686 (2012); A.V, Chubukov, *Itinerant electron scenario for Fe-based superconductors*, Springer Series in Materials Science, Volume 211, 255-329 (2015).
[41] Ar. Abanov, A.V. Chubukov, and J. Schmalian, Advances in Physics **52**, 119 (2003).
[42] S. Avci et al., Nat. Commun. 5, 3845 (2014); A. E. Bohmer, F. Hardy, L. Wang, P. Burger, T. Wolf, P. Schweiss, and C. Meingast, arXiv:1412.7038; X.Wang, J. Kang, and R.M. Fernandes, Phys.Rev.B 91, 024401 (2015); J. Kang, X. Wang, A. V. Chubukov, and R. M. Fernandes, Phys. Rev. B 91, 121104(R) (2015).
[43] V. Stanev, J. Kang, and Z. Tesanovic, Phys. Rev. B 78, 184509 (2008).
[44] E. Demler, H. Kohno, and S.-C. Zhang, Phys. Rev. B **58**, 5719 (1998); W. C. Lee et al., Phys. Rev. B **77**, 214518 (2008); C. Lee and A.H. MacDonald, ibid. **78**, 174506 (2008); I. Fomin, P. Schmitteckert, and P. Wo?lfle, Phys. Rev. Lett. **69**, 214 (1992); Z. Hao and A. Chubukov, Phys. Rev. B **79**, 224513 (2009).
[45] A. Hinojosa, A. V. Chubukov, P. Wölfle, Phys. Rev. B **90**, 104509 (2014).
[46] M. M. Korshunov and I. Eremin, Phys. Rev. B **78**, 140509 (2008); T. A. Maier and D. J. Scalapino, Phys. Rev. B **78**, 020514 (2008).
[47] V. Cvetkovic and O. Vafek, Phys. Rev. B **88**, 134510 (2013).

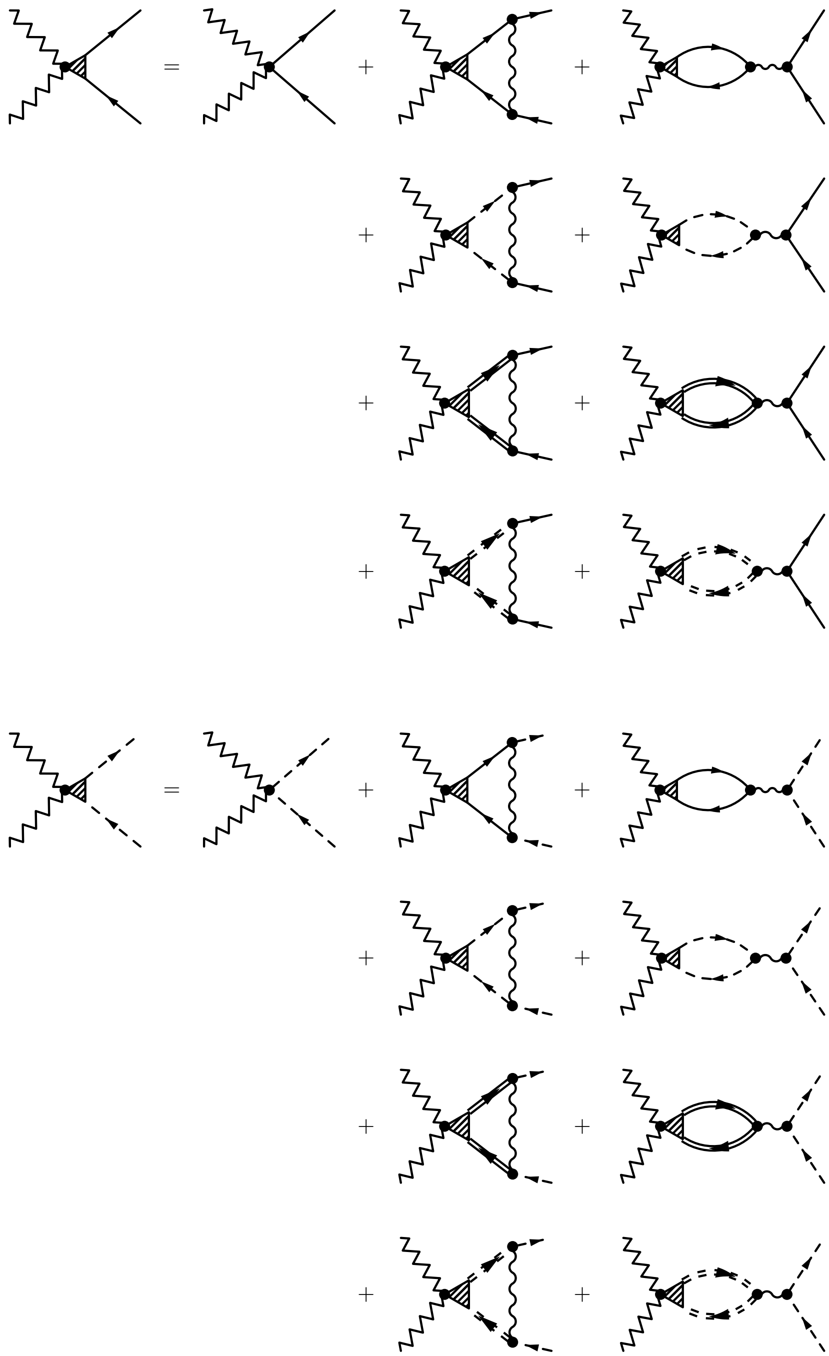

Figure 17. Vertex renormalization for hole bands α and β. The single solid and dashed lines represent excitations from hole bands α and β, respectively, and the double solid and dashed lines from electron bands η and δ, respectively.

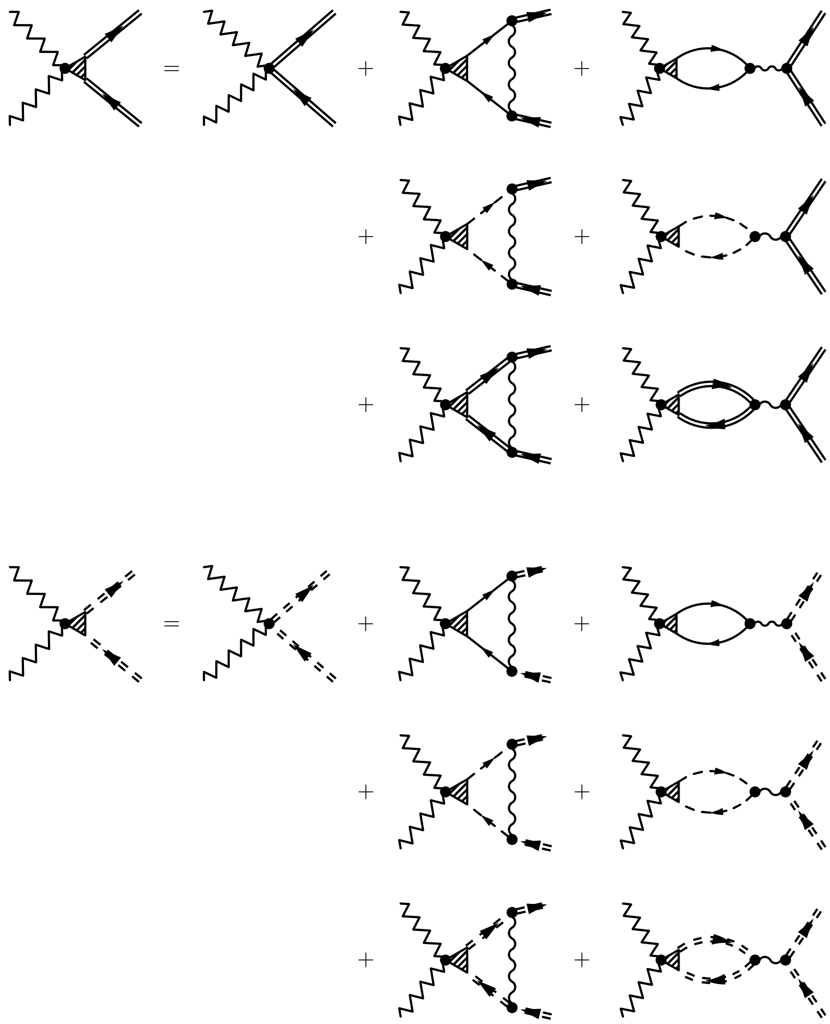

Figure 18. Vertex renormalization for electron bands η and δ. The notations are the same as in Fig. 17.